Lakes_CCI+ - Phase 2. D2.2. Algorithm Theoretical Basis Document (ATBD)

Reference: CCI-LAKES2-0012-ATBD

Issue: 2.1.1 – 17/10/2023

Contract number: 4000125030/18/I-NB –Lakes_cci

11 rue Hermès, Parc Technologique du Canal — 31520 Ramonville Saint-Agne, France
Tel +33 (0)5 61 39 47 00 Fax +33(0)5 61 75 10 14
www.cls.fr

CHRONOLOGY ISSUES

Revised issue	Legacy issues	Date	Objective	Written by
1.0	1.0	09/12/2019	Initial Version	S. Simis et al.
	1.1	24/03/2020	Revision following ESA review	S. Simis et al.
	1.2	24/04/2020	Revision following 2nd ESA review	S. Simis et al.
	2.0	30/07/2020	Update of the LSWT chapter to take into account MODIS data. Update 4. 2: Optical LWE Estimates	C. Merchant, H. Yesou
	2.1	29/09/2020	Revision following ESA Review	J-F Crétaux, H. Yésou, C. Merchant
	2.2	17/03/2021	Update due to the new algorithm implemented for LIT and used for the CRDP version 1.1	C. Duguay
	2.3	30/03/2021	Minor corrections following the ESA Review	B. Coulon
2.0	3.0	03/05/2022	Accompanying CRDP v2.0	All authors
	3.1	06/07/2022	Revision following ESA Review	Laura Carrea
2.1	-	21/07/2023	Updates with CRDP v2.1 Addition of Lake Ice Thickness	S. Simis, L. Carrea, B. Calmettes, J-F Crétaux, C. Duguay, X. Liu, A. Mangili, D. Müller, H. Yésou
2.1.1		17/06/2013	New version after ESA review	S. Simis, L. Carrea, B. Calmettes, J-F Crétaux, C. Duguay, X. Liu, A. Mangili, D. Müller, H. Yésou

Note: versioning prior to 2022 did not follow the CRDP release sequence. The revised versioning in the first column should be used for future consistency.

Checked by	Stefan Simis – PML J-F Cretaux - LEGOS	Stefan Simis Jean-francois Cretaux
Approved by	Alice Andral - CLS	A. Andral
Authorized by	Clément Albergel - ESA	Clement Albergel

DISTRIBUTION

Company	Names	Email
ESA	Clément Albergel	clement.albergel@esa.int
BC	Carsten Brockman	carsten.brockmann@brockmann-consult.de
BC	Dagmar Müller	dagmar.mueller@brockmann-consult.de
BC	Jorrit Scholze	jorrit.scholze@brockmann-consult.de
BC	Kerstin Stelzer	kerstin.stelzer@brockmann-consult.de
BC	Martin Boettcher	martin.boettcher@brockmann-consult.de
BC	Olaf Danne	olaf.danne@brockmann-consult.de
CLS	Alice Andral	aandral@groupcls.com
CLS	Anna Mangilli	amangilli@groupcls.com
CLS	Beatriz Calmettes	bcalmettes@groupcls.com
CLS	Nicolas Taburet	ntaburet@groupcls.com
CLS	Christophe Fatras	cfatras@groupcls.com
CLS	Pierre Thibault	pthibaut@groupcls.com
CNR	Claudia Giardino	giardino.c@irea.cnr.it
CNR	Mariano Bresciani	bresciani.m@irea.cnr.it
CNR	Monica Pinardi	pinardi.m@irea.cnr.it
CNR	Marina Amadori	amadori.m@irea.cnr.it
CNR	Rossana Caroni	caroni.r@irea.cnr.it
CNR	Giulio Tellina	tellina.g@irea.cnr.it
H2O Geo	Claude Duguay	claude.duguay@h2ogeomatics.com
H2O Geo	Yuhao Wu	mark.wu@h2ogeomatics.com
H2O Geo	Jaya Sree Mugunthan	jayasree.mugunthan@h2ogeomatics.com
H2O Geo	Justin Murfitt	justin.murfitt@h2ogeomatics.com
HYGEOS	François Steinmetz	fs@hygeos.com
LEGOS	Jean-François Cretaux	jean-francois.cretaux@cnes.fr
LEGOS	Paul-Gérard Gbektom	paul.gerard.gbetkom@legos.obs-mip.fr
PML	Stefan Simis	stsi@pml.ac.uk
PML	Xiaohan Liu	liux@pml.ac.uk
PML	Nick Selmes	nse@pml.ac.uk
PML	Mark Warren	mark1@pml.ac.uk
Sertit	Hervé Yésou	Herve.yesou@unistra.fr
Sertit Sertit	Jérôme Maxant Sabrina Amsil	maxant@unistra.fr s.amzil@unistra.fr
Sertit	Rémi Braun	remi.braun@unistra.fr
UoR	Chris Merchant	c.j.merchant@reading.ac.uk
Bangor	Iestyn Woolway	iestyn.woolway@bangor.ac.uk
UoR	Laura Carrea	l.carrea@reading.ac.uk
UoS	Dalin Jiang	dalin.jiang@stir.ac.uk

UoS	Evangelos Spyrakos	evangelos.spyrakos@stir.ac.uk
UoS	Ian Jones	ian.jones@stir.ac.uk

LIST OF CONTENTS

1 Introduction 7
2 Lake Water level – LWL 8
2.1 Description of the algorithm and data/satellite used 8
2.2 Algorithm definition 8
2.3 Quality assessment 9
2.4 Summary of strengths, weaknesses and limitations 10
2.5 References 10
3 Lake water extent -LWE 12
3.1 Description 12
3.2 Algorithm definition 12
3.3 Quality assessment 14
3.4 Summary of the strengths, weaknesses and limitations 15
3.5 References 15
4 Lake surface water temperature – LSWT 16
4.1 Description 16
4.2 Algorithm definition 17
4.2.1 Water detection 17
4.2.2 LSWT retrieval 19
4.2.3 Quality levels 19
4.2.4 Remapping (L3U) 20
4.2.5 Daily Collation (L3C) 20
4.2.6 Inter-sensor adjustment (L3S) 21
4.3 Quality assessment 21
4.4 Summary of the strengths, weaknesses and limitations 21
4.5 References 22
5 Lake water-leaving reflectance – LWLR 23
5.1 Description 23
5.2 Algorithm definition 24
5.2.1 Algorithm assumptions and known limitations 29
5.2.2 Specific algorithms for LWLR 29
5.3 Input products and dependencies 38
5.4 Output product 38

5.5 Quality Assessment 38
5.5.1 Atmospheric correction 39
5.5.2 Weighted blending of biogeochemical variable algorithms 40
5.6 Summary of strengths, weaknesses and limitations 41
5.7 References 42
6 Lake Ice cover – LIC 45
6.1 Description 45
6.2 Algorithm definition 45
6.2.1 Input Data 48
6.2.2 Output Data 48
6.2.3 Retrieval Algorithm 48
6.3 Quality assessment 50
6.4 Summary of the strengths, weaknesses and limitations 50
6.5 References 51
7 Lake Ice Thickness- LIT 52
7.1 Description 52
7.2 Algorithm definition 53
7.2.1 Step 1: Optimisation and best fit parameters 54
7.2.2 Step 2: Parameters estimation and LIT retrieval 54
7.3 Quality assessment 55
7.3.1 Quality checks 55
7.3.2 Validation 55
7.4 Summary of the strengths, weaknesses and limitations 58
7.5 References 59

LIST OF TABLES AND FIGURES

Table 1 - List of the instruments used for LSWT4.3 16
Table 2: Thresholds test for water detection 18
Table 3: Quality level criteria 19
Table 4: Chlorophyll-a algorithms per optical water type for MERIS 32
Table 5: Chlorophyll-a algorithms per optical water type for MODIS 34
Table 6: Coefficients of OCX algorithms for each assigned OWT 35
Table 7: Suspended matter algorithms per optical water type for MERIS 36
Table 8: Suspended matter algorithms per optical water type for MODIS 37
Table 9: Output variables in LIC product 48
Table 10: List of lakes for LIC algorithm development and (internal) validation 49

Figure 1: Optical Water Extraction Workflow 13

Figure 2: Detailed workflow of the water extraction procedure within ExtractEO 14

Figure 3: Resulting hypsometry for the lake Bagre in Africa using a set of 26 Sentinel-2 images and LWL time series.. 14

Figure 4: Major steps in LSWT processing 17

Figure 5: Schematic overview of the Calimnos processing chain for LWLR, chlorophyll-a and turbidity or suspended matter. Note that the spectrum selection step is not yet implemented and expected earliest in CRDP v3.0. 24

Figure 6 Climatologic clusters generation and the scoring system. 27

Figure 7 Climatologic consistency flags generation. 28

Figure 8: POLYMER v4.12 matchups of MERIS with in situ reflectance data in LIMNADES, using a ±3 day matchup window and 3x3 pixel extraction window. 39

Figure 9: POLYMER v4.12 matchups of MODIS with in situ reflectance data in LIMNADES, using a ±3 day matchup window and 3x3 pixel extraction window. 40

Figure 10: Comparison of the performance of (left) the best chlorophyll-a algorithm for the predominant optical water type of each lake and (right) per-pixel selection and blending of the two highest ranking algorithms based on optical water type membership scores. 41

Figure 11: Overview of the processing chain for generation of MODIS LIC daily product. RF stands for random forest 47

Figure 12: Geographical distribution of lakes used for LIC algorithm development and validation 49

Figure 13: Comparison of classification accuracies (%) obtained with different band configurations across classifiers. The 7-band combination using RF is the one retained for generation of the LIC v2.1 product (Wu et al., 2021) 50

Figure 14: Example of LRM radar echogram (left) and waveforms (right) over the iced-covered Great Slave Lake. Jason-3 data (pass 45, cycle 148, February 2020). 52

Figure 15: Major steps of the LIT processing 54

Figure 16: Example of LIT estimation as a function of the latitude along Jason-2 track 45 over the Great Slave Lake (top panel) and the associated reduced chi2 goodness of fit statistics (bottom panel) 55

Figure 17: Validation of the LIT estimation with the LRM_LIT retracker on Jason-like simulations. In the left column are shown Jason-like waveform simulations corresponding to the winter-like SIM1 waveforms (top) and to the summer-like SIM2 waveforms. In the right column are shown LIT histograms computed for the winter-like simulations SIM1 (top panel) and for the summer-like simulations SIM2 (bottom panel). The blue lines correspond to the Gaussian fit of the histograms. The input values used to generate the simulations are also shown as dashed black lines. 56

Figure 18: LIT estimates over Great Slave Lake for the 2015-16 winter season. Shown are a comparison between LIT estimates with the LRM_LIT retracker from Jason-2 (triangles) and Jason-3 (stars) data, CLIMo simulations (diamonds) and in situ data (circles). The shaded areas correspond to the LIT estimation uncertainties computed from Jason-2 data (blue) and Jason-3 data (red). Three different realizations of CLIMo simulations are shown by varying the amount of snow on the ice. The in-situ data consist of ice thickness measurements collected in Back Bay near Yellowknife. 57

Figure 19 Evolution of Jason-2 LIT estimates over Great Slave Lake along track 45 for WS3 (winter season 2015-2016). Plots in the left column show, from top to bottom, along-track Jason-2 LIT estimates superimposed on MODIS images on the same date or within one day in December, February, March and end of April. Plots in the right column show the evolution of the Jason-2 LIT estimates as a function of latitude (top plots) and of the reduced chi-squared statistics as a function of the latitude(bottom plots) along the track. 58

1 Introduction

This Algorithm Theoretical Basis Document (ATBD) describes the methodology, theoretical basis, assumptions and limitations of the algorithms used to derive the Lakes_CCI ECV products from input satellite data for the Lakes_cci.

The ATBD details, as applicable for each part of the Lakes_CCI ECV:

- input satellite and ancillary data
- retrieval algorithms used, including:
    - the physical theory used as a basis
    - the mathematical, logical and heuristic procedures employed
    - simplifying assumptions made
- a general overview of the processing chain for retrieval of the data products
- any pre-processing or post-processing steps
- sensor specific optimisations of the algorithm
- steps taken to ensure consistency between products derived from different satellite instruments, where applicable
- approach to harmonisation of products from different instruments, where applicable
- approach to data merging, if performed
- how product uncertainties are estimated on a per-datum prognostic basis, reflecting the combination of sources of uncertainty identified in the E3UB.
- Overall strengths and weaknesses or limitations of the product that are traceable to the algorithm/processing

2 Lake Water level – LWL

2.1 Description of the algorithm and data/satellite used

Altimetry was originally designed for oceanography in the 1970s, and to study favourable continental surfaces, especially in hydrology and glaciology, two themes for which monitoring the height of water or ice surfaces is crucial. The principles of measurement have not changed over time, but the interpretation of measurements becomes more complex with increasing heterogeneity of the target, or the presence of slopes. Altimetry is not a singular measurement - multiple sensors on board an 'altimetry mission' satellite contribute to the quality of the measurement. Accurate orbit positioning sensors are crucial, as well as radiometers to determine the influence of atmospheric moisture on the signal. Dual-frequency altimeter systems for correcting the ionospheric delay are combined onto the same platform to gain the required precision in height measurement. However, these auxiliary sensors do not work for all continental surfaces as they do on ocean surfaces. This chapter, therefore, discusses the proposed solution for the challenge of altimetry of lake surfaces.

Satellite altimeters are designed to measure the two-way travel time of short radar (or laser) pulses reflected from the Earth's surface which gives the distance between the satellite and the reflected surface, called "range". The shape of the reflected signal, known as the "waveform", represents the power distribution of accumulated echoes from the radar pulse hitting the surface. The so-called onboard tracking system is the software which attempts to keep the reflected radar echo within the receiver observation window. The resulting waveforms are called 'tracked waveforms'. The travel time is calculated using a predefined analytic function, which fits the time distribution of the reflected energy. The fitting process of the acquired waveform is called re-tracking. The first altimetry missions were designed for the ocean domain and the corresponding algorithm, the so-called Brown model (Brown 1977) was fitted to classic ocean surfaces. This considers that thermal noise is followed by a rapid rise of the returned power called 'leading edge', and a gentle end sloping plateau known as 'trailing edge'. However, over the continents the waveforms are generally contaminated by noise resulting from multiple land returns such as vegetation, bare soil, or steep shorelines. Consequently, the shape of the echoes reflected by continental waters is often very different from that reflected by the ocean surface. It can thus become complex, if not impossible, to unambiguously calculate the water level of a river or small lake using the classic Brown analytic function. One way of working around this is to use alternative and more suitable re-tracking functions of the waveforms. Moreover, several corrections that are commonly well measured over ocean are also degraded over continental surface and lead to use specific models.

2.2 Algorithm definition

Here, Lake Water Level (LWL) is measured using satellite radar altimetry (alternatively, Lidar altimetry, for example on ICESat-1 and ICEsat-2 missions, can also be considered).

Radar altimeters send an electromagnetic pulse to the satellite nadir and record the propagation time to and from the emitted wave and its echo from the surface. The electromagnetic bands of interest are the Ku and Ka bands, with are reflected perfectly – without penetration – by water (which is not the case for snow and ice). Multiplied by the speed of light c, half the time it takes for the transmission Δt gives length R (the range) between the satellite and the reflective surface:

$$R = c \frac{\Delta t}{2} \qquad [3.1]$$

The height *H* of the reflective surface is given by the following equation:

$$H = a - (R + \Sigma C_p + \Sigma C_g) \qquad [3.2]$$

where *a* is the orbital altitude of the satellite with respect to the ellipsoid. Corrections must be made for propagation in the atmosphere (C_p) and also vertical movements of the Earth's crust (C_g).

The ellipsoidal height is then converted into elevation *h*, taking the local undulation of geoid N into account:

$$h = H - N \qquad [3.3]$$

The ΣC_p and ΣC_g terms in Equation 3.2 correspond to sets of corrections that must be subtracted to arrive at an accurate estimation of H.

There are two types of corrections:

- propagation corrections needed because the radar pulse propagates through the atmosphere at a speed below the speed of light c used in Eq. 4.1
- geophysical corrections linked to the vertical movements of the Earth surface (tides, for example) and for which we want to correct the measurement in order to apply it to a fixed geodetic datum in the terrestrial reference frame.

Finally, we can express the height of a lake by the full following equation:

$$h = a - R - DTC - WTC - IC - ET - PT - LT - SSB - N \qquad [3.4]$$

where DTC is the dry tropospheric correction, WTC the wet tropospheric correction, IC the ionospheric correction, ET the Earth tide, PT the polar tide, LT the lake tide and SSB the instrumental so-called sea state bias. In the case of inland water products, these geophysical corrections come from models and are provided in the altimetry datasets. For some past missions, a temporal interpolation may be required.

2.3 Quality assessment

Quality assessment is carried out by comparing the retrieved LWL with independent in situ measurements. In situ measurements are available for some lakes on national hydrological services, for example in Canada or Brazil, for selected lakes and reservoirs, or they are released to the project team by the State Hydrological Institute of St Petersburg within the framework of the Hydrolare data centre. A set of approximately 20 lakes regularly serve as validation data sets for altimetry products. The accuracy of lake height measurement depends on several factors: range, orbit and correction errors. Range errors result from surface roughness and quality of the retracking of the altimeter waveform. It is also important to emphasize that the altimeter measurement is an average over the footprint which intrinsically differs from a single point measurement of a ground gauge, and which is furthermore generally done along the coastline.

Performing comparisons over a set of several lakes and reservoirs of varying morphology and from different regions addresses the recurring question of accuracy of altimetry for lakes and reservoirs and its dependency on the size of the water bodies. It is not clear whether a minimum size threshold exists below which the altimeter does not provide valid water levels. Past studies (see Cretaux et

al. 2016) have shown that the accuracy of LWL is largely sub-decimetre for large lakes and that lake size influences the quality of the measurement. However, these results also show that accuracy is dependent on the lake environment: mountain lakes or those with ice and snow in winter, as well as large but narrow reservoirs have degraded accuracy. For Lake Onega for example, the RMS accuracy was twice as good when winter months were excluded compared to the year as a whole. Past studies further show that accuracy of LWL products ranges from a few centimetres for very large lakes to a few decimetres for small or narrow lakes (Ričko et al. 2012, Cretaux et al. 2016). However, new missions like the Sentinel-3 constellation present new technological developments from which improved accuracy have been largely demonstrated (Boy et al., 2022; Taburet at al., 2020; Quartly et al., 2020), owing to acquisition in SAR mode. This will have little effect for large lakes (Cretaux et al. 2016) but prompts new assessment to gauge the extent of improvements over smaller lakes.

2.4 Summary of strengths, weaknesses and limitations

Since LWL products are exclusively based on satellite altimetry, its coverage depends on the satellite constellation, which present some limitations since some lakes will only occasionally be observed, while other lakes are never found under the altimeter track.

Since the launch of Topex / Poseidon in 1992, radar altimetry has evolved a lot from low resolution mode to SAR mode, from Ku band to Ka Band (Saral/Altika), which leads to disparity in the quality of the time series from one lake to another one, and for lakes covered by several altimeters. This is particularly true for small or narrow lakes, for which the SAR mode is more adapted and allows calculating more precise time series.

With the SWOT mission, which has a full coverage of the continent following requirements to resolve all lake levels, extent, and volume changes for lakes bigger than 6 ha, we expect much better results and we would be able to provide LWL for all lakes in the database in future.

The strength of satellite altimetry is that it is perennial (with current and future constellation of sentinel-3, sentinel-3NG, sentinel-6, SWOT, Icesat-2). Moreover, radar altimetry is not affected by cloud coverage.

With more than 30 years of altimetry data processing, the technique is robust, and many improvements have been progressively implemented in the data processing over lakes. LWL products then can serve as input for LWE inferring potential global studies on lake storage changes (Yao et al., 2023).

2.5 References

Birkett C. M. (1995). Contribution of TOPEX/POSEIDON to the global monitoring of climatically sensitive lakes, Journal of Geophysical Research, 100, C12, 25, 179-25, 204

Boy F., Cretaux J-F., Boussaroque M., & Tison C. (2022). Improving Sentinel-3 SAR mode processing over lake using numerical simulations, IEEE Transactions on Geoscience and Remote Sensing, 60, 1-18, Art no. 5220518, Doi: 10.1109/TGRS.2021.3137034

Brown G. S. (1977). The Average Impulse Response of a rough surface and its applications, IEEE Trans. Antennas Propag, Vol. 25, pp. 67-74. 10.1109/TAP.1977.1141536

Crétaux J-F. and Birkett C. M. (2006). Lake studies from satellite altimetry, C R Geoscience, 10.1016/J.crte.2006.08.002

Crétaux J-F. Calmant S. Romanovski V. Perosanz F. Tashbaeva S. Bonnefond P. Moreira D. Shum C. K. Nino F. Bergé-Nguyen M. Fleury S. Gegout P. Abarca Del Rio R. Maisongrande P. (2011). Absolute Calibration of Jason radar altimeters from GPS kinematic campaigns over Lake Issykkul, Marine Geodesy, 34: 3-4, 291-318, 10.080/01490419.2011.585110

Crétaux J-F, Abarca Del Rio R. Berge-Nguyen M. Arsen A. Drolon V. Clos G. Maisongrande P. (2016). Lake volume monitoring from Space, Survey in geophysics, 37: 269-305. 10.1007/s10712-016-9362-6

Crétaux J-F. Bergé-Nguyen M. Calmant S. Jamangulova N. Satylkanov R. Lyard F. Perosanz F. Verron J. Montazem A. S. Leguilcher G. Leroux D. Barrie J. Maisongrande P. and Bonnefond P. (2018). Absolute calibration / validation of the altimeters on Sentinel-3A and Jason-3 over the lake Issykkul, Remote sensing, 10, 1679. 10.3390/rs10111679

Quartly, G.D.; Nencioli, F.; Raynal, M.; Bonnefond, P.; Nilo Garcia, P.; Garcia-Mondéjar, A.; Flores de la Cruz, A.; Crétaux, J.-F.; Taburet, N.; Frery, M.-L.; Cancet, M.; Muir, A.; Brockley, D.; McMillan, M.; Abdalla, S.; Fleury, S.; Cadier, E.; Gao, Q.; Escorihuela, M.J.; Roca, M.; Bergé-Nguyen, M.; Laurain, O.; Bruniquel, J.; Féménias, P.; Lucas, B. (2020). The Roles of the S3MPC: Monitoring, Validation and Evolution of Sentinel-3 Altimetry Observations. Remote Sens. 12, 1763. doi:10.3390/rs121111763

Ričko M. C. M. Birkett, J. A. Carton, and J-F. Cretaux. (2012). Intercomparison and validation of continental water level products derived from satellite radar altimetry, J. of Applied Rem. Sensing 6, Art N°: 061710.10.1117/1.JRS.6.061710

Taburet N., Zawadzki., Vayre M., Blumstein D., LE Gac S., Boy F., Raynal M., Labroue S., Cretaux J-F., and Femenias P. (2020). S3MPC: Improvement on inland water tracking and water level monitoring from the OLTC onboard Sentinel-3 altimeters, Remote Sensing 12, 18, AN 3055, Doi: 10.3390/rs12183055

Yao F., Ben Livneh B., Rajagopalan B., Wang J., Crétaux J-F., Wada Y., Berge-Nguyen M. (2023). Satellites reveal widespread decline in global lake water storage, *Science* 380, 743-749.

3 Lake water extent -LWE

3.1 Description

Lake Water Extent (LWE) can be expressed as the outline of a water body (a shape) or as the total areal extent of a waterbody (a single quantity). It is practically very challenging to process the high spatial resolution satellite imagery required to generate maps of water presence for hundreds, if not thousands, of lakes at the accuracy and temporal frequency required for climate studies. For this reason, the strategy adopted is twofold. First, for each lake, we collect satellite imagery spread out over a long time period. To choose the images we use the water level time series (calculated using satellite altimetry) to determine when the lake was at low, medium, and high level. A relationship (a first or second order polynomial) can then be established using a set of 10 to 15 data combinations of LWL and LWE and least square adjustment. We can then relate LWL from altimetry to LWE using the established so-called hypsometric relation. This allows us to achieve a high temporal resolution of both LWL and LWE without overwhelming image processing requirements. The relationship is stable over long periods of time if the geomorphology of the lake and immediate surrounding landscape does not markedly change.

LWE maps used to calculate the hypsometry coefficients are determined from contrasts in the optical reflectance of water compared to surrounding land. Water surfaces are detected using a multilayer perceptron (neural network) algorithm and integrating the GSW database for sampling. This processing chain is implemented as part of a processing chain for Sentinels 1-3 used to derive several properties including water, fire, and cloud detection, in time series context with large spatial and temporal windows.

3.2 Algorithm definition

To calculate the LWE we use the vector (ΔLWL, LWE) derived from corresponding altimetry and water extent observations to estimate, by least square adjustment, the coefficients representing the polynomial subsequently used as hypsometry curve. LWL is then used together with the hypsometry coefficient to determine the LWE variable. This procedure is detailed as follows.

We first use the water level time series inferred from satellite altimetry and released as LWL products, to determine key periods when the lake was at extreme heights, as well as some intermediate values. Satellite images are then selected for the same dates for water mask detection using approaches described above. It is not realistic to determine water extent of a lake for each measurement of its water level, especially when a lake is too large and is not covered by only one image. We select between 10 and 20 images at different dates and calculate the hypsometry relationship (LWE/dLWL) which is then applied to determine surface extent of the lakes each time a water level is calculated using satellite altimetry. The hypsometry is expressed as a polynomial of degree 1, 2 or 3 depending on the linearity of the couples of water level and surface extent of the lake. In such processing, we do not need to process a large amount of satellite images, and this is a practical way to produce lake surface extent together with lake water level. We do not extrapolate the water surface for water height outside of the maximum and minimum values used to determine polynomial coefficients. Therefore, we try to collect satellite images as close as possible to the maximum and minimum level observed from satellite altimetry. The method is applied and described in Cretaux et al. (2015, 2016).

In a previous, dedicated Lakes_cci effort, various methods for image based LWE determination were compared, using both optical and radar methods. Based on the results of inter-comparison on a small set of lakes with increasingly complex hydromorphology, an approach based only on optical HR imagery was adopted. Water surfaces were extracted from the images based on the exploitation of an in-house processing chain (Figure 1), named ExtractEO (Maxant et al, 2022).

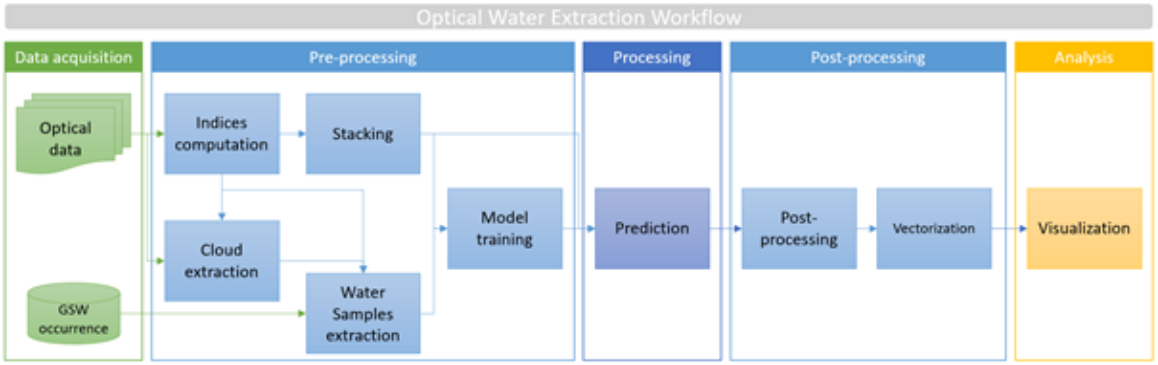

Figure 1: Optical Water Extraction Workflow

The preprocessing steps correspond to:

- Region Of Interest (ROI) is defined including the target lake.
- Selection of set of images representative of the different water levels of the target, i.e. based on altimetric water level curves from Hydroweb.

The processing then follows the scheme shown in Figure 2:

- Automatic water sample generation from Global Surface Water. Water indices are computed to remove outliers and filter the training samples to the hydrological reality of the image (water extent, resolution)
- Training using the Multi-Layer Perceptron classifier
- Slope and hillshade thresholds derived from HR DEMs are applied to refine the water extraction (post-processing)
- Minimum mapping unit (MMU) sieving to remove small features (0,1 hectares in this case)
- Water extent (in km^2) is subsequently calculated using the sum of individual pixel classified as water pixel within the ROI
- Generation of a max extent water mask

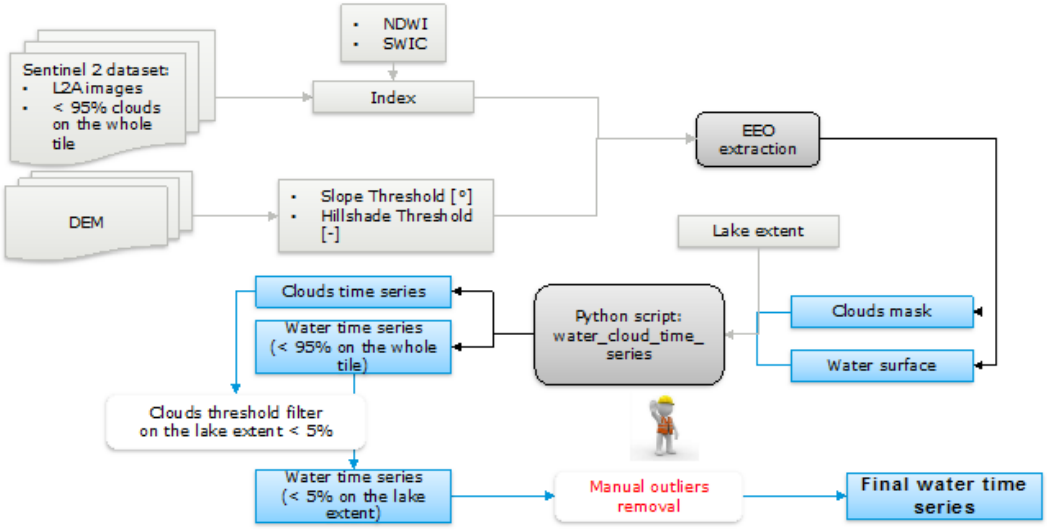

Figure 2: Detailed workflow of the water extraction procedure within ExtractEO

From a first set of selected images/dates, after outlier removal, 10 to 20 images are retained to calculate the hypsometry relationship.

3.3 Quality assessment

A final estimation of accuracy is calculated on all vectors used to calculate the hypsometry coefficients. The hypsometry is represented by a linear or a quadratic polynomial, depending on lake morphology, and is estimated using a set of 10-15 vectors (LWL, LWE) for a selection of dates at different levels. A way to estimate the associated uncertainty is to calculate the RMS of the differences between the theoretical (calculated from hypsometry's coefficient) and the measured LWE (directly from satellite imagery) for the dates that have been chosen to build the hypsometry. A series of tests done over a set of 40 lakes have shown that the estimated RMS of LWE was lower than 2 % of the total extent for each of the 40 lakes.

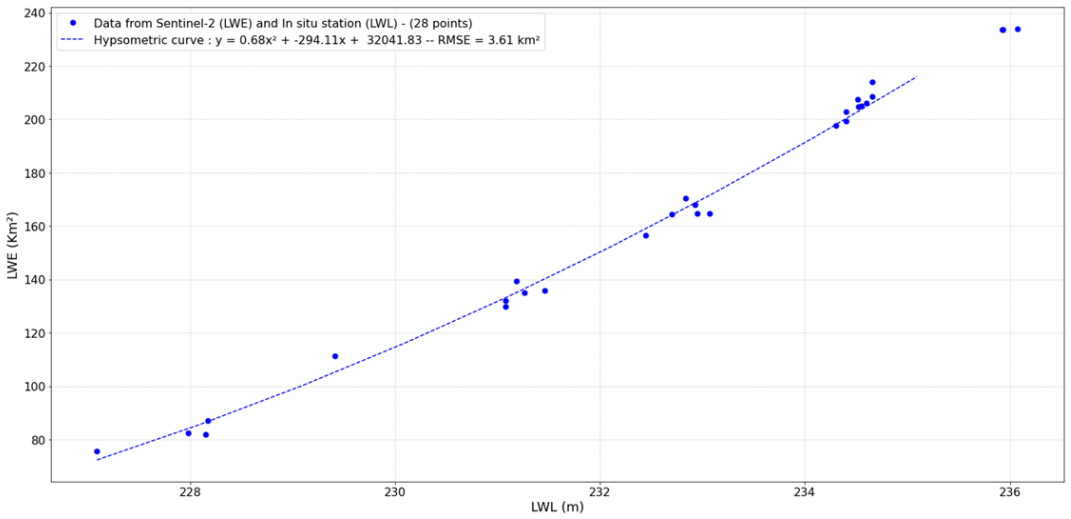

Figure 3: Resulting hypsometry for the lake Bagre in Africa using a set of 26 Sentinel-2 images and LWL time series..

3.4 Summary of the strengths, weaknesses and limitations

Strengths:

- A robust and proved method
- RMS meets the target requirements

Weaknesses:

- Access to input data timeseries, i.e. Landsat for early observations and Sentinel-2 for recent observations, can be a bottleneck. Limited access to the full Sentinel archives through the European DIAS providers is solved by using a FORCE gateway or the AWS capabilities.
- Availability of cloud-free optical data
- Gaps in the satellite archive (i.e. Landsat 7)
- Time consuming process to reach the required fine adjustment of the hypsometric curves

Limitations:

- There are (few) lakes for which there is no correspondence between surface extractions and corresponding elevation values.
- Observation limitations with mountainous deep lakes, with sharp banks, showing limited surface area expansion when waters rise.
-

3.5 References

Cretaux J-F. Biancamaria S. Arsen A. Bergé-Nguyen M. and Becker M. (2015). Global surveys of reservoirs and lakes from satellites and regional application to the Syrdarya river basin, *Environmental Research Letter*, 10, 1, AN: 015002. doi: 10.1088/1748-9326/10/1/015002

Crétaux J-F, Abarca Del Rio R, Berge-Nguyen M, Arsen A, Drolon V, Clos G, Maisongrande P. (2016). Lake volume monitoring from Space, *Survey in geophysics*, 37: 269-305, Doi 10.1007/s10712-016-9362-6

Maxant J, Braun R, Caspard M, Clandillon S. (2022). ExtractEO, a Pipeline for Disaster Extent Mapping in the Context of Emergency Management. Remote Sensing. .14(20):5253. https://doi.org/10.3390/rs14205253

McFeeters S. K. (1996) The use of Normalized Difference Water Index (NDWI) in the delineation of open water features, International Journal of Remote Sensing, 17(7):1425–1432

4 Lake surface water temperature – LSWT

4.1 Description

This section describes the algorithm for Lake Surface Water Temperature (LSWT) production chain. For consistency with data produced in heritage projects, the version (v4.5) described here refers to the scientific versioning of the climate data record in a manner already familiar to users of data from previous projects, with GloboLakes offering the product generation as v4.0 (Carrea et al. 2019) and the first version from Lakes_cci being termed v4.1.

The algorithm described here is consistent with the v4.1 algorithm described in ATBD v1.0, with the exception of the following advances:

- V4.5 includes data from the Moderate-resolution Imaging Spectroradiometer (MODIS) on Terra processed with ERA-5 (the most recent numerical weather prediction, NWP, re-analysis from ECMWF)
- V4.5 includes data from the Sea and Land Surface Temperature Radiometer (SLSTR) on Sentinel3A And Sentinel3B processed with the ECMWF operational meteorological files contained in the L1b SLSTR files.

The inclusion of the MODIS with ERA-5 data stream and of the SLSTRs improves the data density which is particularly scarce until 2007.

The LSWT climate data record (CDR) is based on the Along-Track Scanning Radiometer (ATSR), Advanced Very High-Resolution Radiometer (AVHRR), SLSTR series and MODIS on Terra instruments. The timeline of the instruments used is summarised in Table 1.

Table 1 - List of the instruments used for LSWT4.3

Instrument/Platform	Start	End	NWP
ATSR2/ERS2	01/06/1995	22/06/2003	ERA-Interim
AATSR/Envisat	20/05/2002	08/04/2012	ERA-Interim
MODIS/Terra	24/02/2000	31/12/2022	ERA5
AVHRR/MetOpA	01/03/2007	31/08/2019	ERA-Interim
AVHRR/MetOpB	13/12/2012	31/08/2019	ERA-Interim
SLSTR/Sentinel3A	01/06/2016	31/12/2022	ECMWF operational
SLSTR/Sentinel3B	21/08/2020	31/12/2022	ECMWF operational

The scope of this algorithm description applies to the following steps:

(1) identification of water-only pixels for valid retrieval,

(2) the LSWT retrieval itself,

(3) estimating the daily average LSWT from the instantaneous skin observation,

(4) assigning a pixel quality level,

(5) remapping the data to a regular global grid,

(6) cross-sensor LSWT harmonization.

4.2 Algorithm definition

The LSWT processing sequence is described in Figure 4. The individual processing steps are described in turn below.

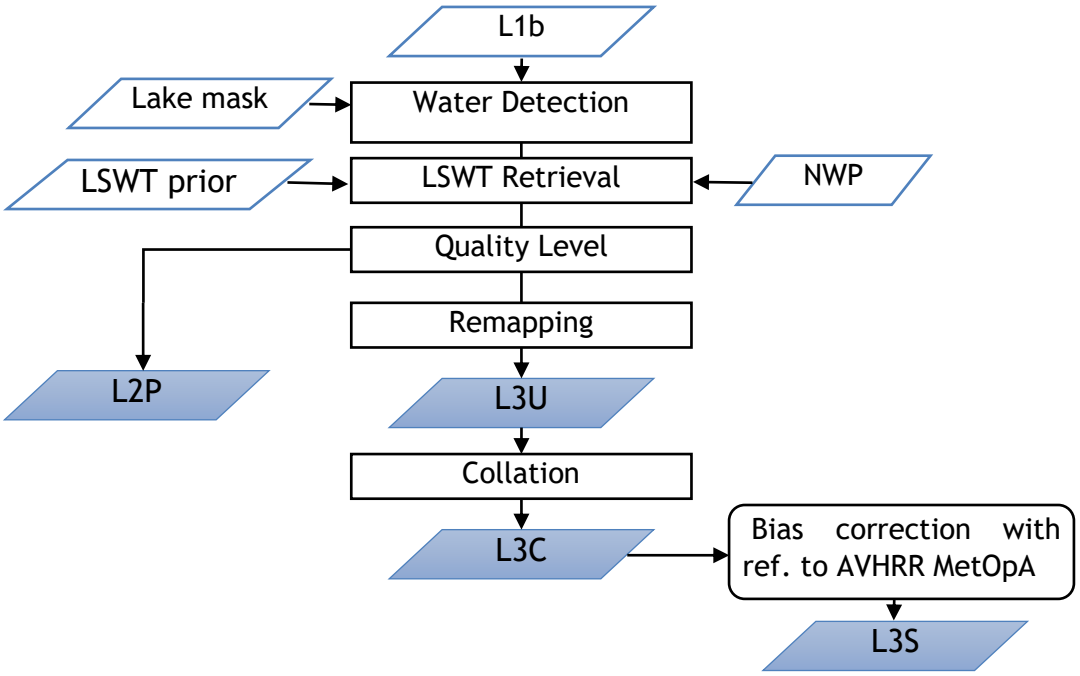

Figure 4: Major steps in LSWT processing

4.2.1 Water detection

Water detection is applied to potential inland water pixels. It operates by calculating a score against several metrics, derived from reflectance channels available. For this reason, LSWT products are in this version obtained only from daytime scenes.

The score for a given metric is defined as:

$$s = \begin{cases} 0 & \text{if } X \le t_0 \\ \frac{X - t_0}{t_1 - t_0} & \text{if } t_0 < X < t_1 \\ 1 & \text{if } X \ge t_1 \end{cases} \qquad [4.1]$$

The score is a linear ramp between 0 and 1, similar to well-known concepts of “fuzzy logic” (the scores are like probabilities).

The values of the terms in EQ1 are given in Table 2. The first three metrics based on red, near infra-red and shortwave infra-red bands use the expectation that reflection from a cloud-affected pixel exceeds that from a clear view of a lake, with values appropriate to different wavelengths.

The MNDWI is the modified normalised difference water index. The NDVI is a normalised difference vegetation index. The setting of the thresholds was done (within GloboLakes) using AATSR imagery

tuned to a probability of cloud image derived from MERIS 300 m imagery. The tuning of thresholds was done one-at-time across metrics, maximising the posterior probability that a certain pixel is cloudy or cloud free.

Table 2: Thresholds test for water detection

$\boldsymbol{X}$, metric	Score definition	Thresholds
R_{670}	$s = \begin{cases} 0 & \text{if } X \geq t_0 \\ \frac{X - t_0}{t_1 - t_0} & \text{if } t_1 < X < t_0 \\ 1 & \text{if } X \leq t_1 \end{cases}$	t_0 = 0.132 t_1 = 0.032
R_{870}	$s = \begin{cases} 0 & \text{if } X \geq t_0 \\ \frac{X - t_0}{t_1 - t_0} & \text{if } t_1 < X < t_0 \\ 1 & \text{if } X \leq t_1 \end{cases}$	t_0 = 0.097 t_1 = 0.022
R_{1600}	$s = \begin{cases} 0 & \text{if } X \geq t_0 \\ \frac{X - t_0}{t_1 - t_0} & \text{if } t_1 < X < t_0 \\ 1 & \text{if } X \leq t_1 \end{cases}$	t_0 = 0.048 t_1 = 0.012
MNDWI	$s = \begin{cases} 0 & \text{if } X \leq t_0 \\ \frac{X - t_0}{t_1 - t_0} & \text{if } t_0 < X < t_1 \\ 1 & \text{if } X \geq t_1 \end{cases}$	t_0 = 0.295 t_1 = 0.515
NDVI	$s = \begin{cases} 0 & \text{if } X \geq t_0 \\ \frac{X - t_0}{t_1 - t_0} & \text{if } t_1 < X < t_0 \\ 1 & \text{if } X \leq t_1 \end{cases}$	t_0 = -0.085 t_1 = -0.245
MNDWI-NDVI	$s = \begin{cases} 0 & \text{if } X \leq t_0 \\ \frac{X - t_0}{t_1 - t_0} & \text{if } t_0 < X < t_1 \\ 1 & \text{if } X \geq t_1 \end{cases}$	t_0 = 0.375 t_1 = 0.685

The first three metrics use the expectation that reflection from a cloud-affected pixel exceeds that from a clear view of a lake, with values appropriate to different wavelengths. The MNDWI is the modified normalised difference water index. The NDVI is a normalised difference vegetation index. The setting of the thresholds was done (within GloboLakes) using AATSR imagery tuned to a probability of cloud image derived from MERIS 300m imagery. The tuning of thresholds was done one-at-time across metrics, maximising the posterior probability that a certain pixel is cloudy or cloud free.

The same method will apply for AATSR, AVHRR and MODIS, although the parameter values will be re-evaluated for MODIS. Additionally, to maximise consistency across the Lake_cci project, we expect to use full resolution information from the MODIS LIC processing chain to exclude ice-covered pixels consistently.

4.2.2 LSWT retrieval

The retrieval scheme is the optimal estimation (OE) scheme (MacCallum et al. 2012) for all sensors, the equation for which is:

$$\hat{\boldsymbol{x}} = \boldsymbol{x_a} + \boldsymbol{G}\big(\boldsymbol{y} - \boldsymbol{F}(\boldsymbol{x_a})\big) \quad with \quad \boldsymbol{G} = (\boldsymbol{K}^T\boldsymbol{S}_\varepsilon^{-1}\boldsymbol{K} + \boldsymbol{S}_a^{-1})^{-1}\boldsymbol{K}^T\boldsymbol{S}_\varepsilon^{-1} \qquad [4.2]$$

The retrieved state $\hat{\boldsymbol{x}}$ is the prior state $\boldsymbol{x_a}$ plus an increment of $\mathbf{G}\big(\boldsymbol{y} - F(\boldsymbol{x}_a)\big)$ where F is the forward model, i.e. the radiative transfer model (RTM) runs for the prior re-analysis data and prior LSWT. The matrix $\mathbf{K}$ expresses how the observations change for departures from the prior state x_a, i.e. it is a matrix where a given row contains the partial derivatives of the brightness temperature in a particular channel with respect to each element of the state vector in turn. The partial derivatives are the tangent linear outputs from the forward model $\mathbf{F}$. $\mathbf{S}_\varepsilon$ is the error covariance of the differences between the model and observed brightness temperatures. This error covariance matrix is the sum of the radiometric error covariance in the observations ($\mathbf{S}_o$) and estimated error covariance of the forward model ($\mathbf{S}_m$). $\mathbf{S}_a$ is the error covariance matrix for the prior state variables.

Standard OE theory also enables estimation of the retrieval uncertainty (to be output), a diagnostic of fit (the χ^2 of the retrieval fit) and the sensitivity of the retrieval to the true LSWT ("averaging kernel" in retrieval theory). The latter two outputs are used within quality level attribution (see below).

4.2.3 Quality levels

Quality level is treated as a concept that is distinct from uncertainty: a highly uncertain LSWT can have the highest quality level if all the conditions for giving a valid LSWT and valid LSWT uncertainty are met: the quality level reflects the degree of confidence in the validity of the uncertainty estimate and not the magnitude of data uncertainty.

The quality level assigned to a pixel will be the lowest level (row of table) which matches any of the conditions shown in Table 3. The assignments are compatible with GHRSST conventions: i.e. a particular level is given if none of the conditions higher up any column of the table are met. In the table d is the distance to land.

Table 3: Quality level criteria

Level	Meaning	Water detection score (0. 5<d<=1.5)	Water detection score (d>=1.5)	Sensitivity	χ^2	Other
0	No data	<0	<0			No data; non-lakes pixel
1	Bad data	<0.5	<0	<0.1	>3	LSWT < 273.15
2	Worst quality	<2	<0.5	<0.5	>2	Limb (θ_{sat} > 55)
3	Low quality	<3.5	<2	<0.9	>1	
4	Acceptable quality	<4.5	<3.5		>0.35	

For instance, any pixel where s is unavailable (value is less than zero), required input BTs are unavailable, or which is over land will be assigned quality level of 0. Next, any pixels close to land which have s < 0.5, calculated LSWT sensitivity < 0.1 etc. will be assigned quality level of 1 and so on.

- Quality level 0 pixels should contain no other data
- Quality level 2-5 pixels should always contain valid data
- Quality level 1 pixels contain data, but the data are not suitable for use (bad data). For instance, the LSWT retrieval may have been attempted, but rejected as bad data due to low sensitivity etc

We recommend using quality level 4 and 5, and consideration of use of quality level 3 with caution, depending on the user's application.

4.2.4 Remapping (L3U)

The remapping from the L2 data in swath projection to the fixed L3 grid proceeds as follows:

- Identify L2 pixels contributing to a L3 cell
- Select highest quality level pixel(s) in the L3 cell
- Calculate average LSWT from the pixels that share the highest quality level and propagate uncertainties to the uncertainty in this average (Bulgin et al. 2015a)

When averaging from the pixel scale to L3 grid scale, the component or uncertainty from uncorrelated errors reduces (uncertainty in the mean is scaled by the familiar "$1/\sqrt{n}$"). Uncertainty in the correlated error components is not reduced by averaging, since over these small scales the degree of correlation will be very high and is taken to be perfect ("r = 1"). The total uncertainty in the average is found by combining the propagated component uncertainties.

If the grid cell contains pixels which were not included in the averaging (e. g. due to the presence of cloud etc.), then there is an additional uncertainty due to incomplete sampling. This is calculated following Bulgin et al. (2015b) (derived for application to sea surface temperature uncertainty estimation) and is added to the uncorrelated component.

4.2.5 Daily Collation (L3C)

The polar orbiting satellite carrying the AVHRR/ATSR sensors typically complete 14-15 orbits each day resulting in the same number of L2P or L3U products. While L3U files are on a global grid, they are very sparse as the sensor will only observe a small fraction of the Earth's surface in each orbit. For ease of use the LSWT outputs are collated to produce one file for each 24-hour period, corresponding to day-time observations.

Following the GHRSST conventions [D1], when collating observations from overlapping orbits in the same day the L3C will contain the highest quality observation available in the 24-hour period. The selection of best observation is done as follows:

- Choose input cells with the highest quality level
- If multiple observations have the same quality level, then average.

4.2.6 Inter-sensor adjustment (L3S)

Inter-sensor adjustment applies small adjustment factors to reconcile typical differences between the LSWT obtained from different sensors. This is done by selecting a reference sensor and applying a per-lake adjustment to other sensors. This adjustment is applied only if:

- Enough observations where available to estimate the adjustment for the lake (more than 3 months of data for each sensor-to-reference pair).

The uncertainty of the adjustment was less than 0.049 K for 80% of the lakes.

For MODIS, only LSWTs of quality level 4 and 5 have been used for the final dataset and an overall adjustment of 0.19K and 0.11K for quality level 4 and 5 respectively have been applied.

A flag indicating whether the adjustment has been applied is present in the files and the uncertainty of the bias correction is included in the total uncertainty. For lakes where the flag is not set, the impact of changes in sensor on the long-term trends in LSWT is less well constrained, and trends should be treated with caution.

4.3 Quality assessment

The quality assessment exercise is carried out mainly comparing the retrieved LSWTs with independent in situ measurements. An in-situ database has been compiled and is updated towards the end of each year. Quality control checks are performed on the in-situ data ranging from unrealistic values to comparison with the climatology together with its variability. The lakes where in situ data are available are distributed globally although European and especially North American lakes are the most monitored. The assessment of the differences between reference data and satellite LSWT is carried out using robust statistics which is resistant to outliers and bad data in both satellite and in situ measurements. Each LSWT is accompanied by its uncertainty which will be validated using independent reference data as well.

4.4 Summary of the strengths, weaknesses and limitations

Strengths

- The retrieval of LSWT is based on physics which gives good reason to expect stable performance across domains in time and space that cannot be directly easily validated
- Estimation of the LSWT retrieval uncertainty at pixel level
- Quality levels assigned at pixel levels which summarise the confidence in the LSWT and its uncertainty. They are assigned on the base of the chi2 of the OE retrieval, the water detection score, the closeness to the shore, the satellite zenith angle, and the sensitivity to the prior.

Weakness

- Currently, only LSWT has been retrieved only during daytime. Adding nighttime retrievals would improve the data coverage but also nighttime LSWT are more stable because not influenced by insolation
- The water detection algorithm which is used for detecting water in presence of clouds relies on threshold tests which are applied to visible channels and combinations. Consequently, the thresholds depend on water type and each threshold may be different for each water type. Also, the thresholds depend on wind and satellite zenith angle. In this version of the water detection algorithm a threshold for all the lakes has been derived and utilised

Limitations

- Cloudiness limits the retrieval using infrared/visible channels. Therefore, some parts of the globe have much less coverage due to high cloud cover.
- Resolution of meteorological satellite is ~1km therefore smaller lakes are excluded from the retrieval

4.5 References

Bulgin, C. E. Embury, O. Corlett, G. and Merchant, C. J. (2016a) Independent uncertainty estimates for coefficient based sea surface temperature retrieval from the Along-Track Scanning Radiometer instruments. Remote Sensing of Environment, 178. pp. 213-222. ISSN 0034-4257 doi:10.1016/j.rse.2016.02.022

Bulgin, C. E. Embury, O. and Merchant, C. J. (2016b) Sampling uncertainty in gridded sea surface temperature products and Advanced Very High-Resolution Radiometer (AVHRR) Global Area Coverage (GAC) data. Remote Sensing of Environment, 117. pp. 287-294. ISSN 0034-4257 doi:10.1016/j.rse.2016.02.021

Carrea, L. Embury, O. and Merchant, C. J. (2015a) Datasets related to in-land water for limnology and remote sensing applications: distance-to-land, distance-to-water, water-body identifiers and lake-centre co-ordinates. Geoscience Data Journal, 2(2). pp. 83-97. ISSN 2049-6060 doi:10.1002/gdj3.32

Carrea, L. ; Embury, O. ; Merchant, C. J. (2015b): GloboLakes: high-resolution global limnology dataset v1. Centre for Environmental Data Analysis, 21 July 2015. doi:10.5285/6be871bc-9572-4345-bb9a-2c42d9d85ceb

Carrea, L. ; Merchant, C. J. (2019): GloboLakes: Lake Surface Water Temperature (LSWT) v4. 0 (1995-2016). Centre for Environmental Data Analysis, 29 March 2019. doi:10.5285/76a29c5b55204b66a40308fc2ba9cdb3.

MacCallum, S. N. and Merchant, C. J. (2012) Surface water temperature observations for large lakes by optimal estimation. Canadian Journal of Remote Sensing, 38(1). pp. 25-45. ISSN 1712-7971 doi:10.5589/m12-010

[D1]GHRSST data specification; https://www.ghrsst.org/wp-content/uploads/2016/10/GDS20r5.pdf

5 Lake water-leaving reflectance – LWLR

5.1 Description

Lake water-leaving reflectance is the atmospherically corrected ratio of water-leaving radiance relative to downwelling irradiance, corrected for viewing and sun angle effects. LWLR describes the apparent colour of the water body irrespective of illumination conditions and under the assumption that the water is optically deep. The representation of lake colour is typically a reflectance spectrum, where the shape and amplitude are characteristic of biogeochemically relevant substances, and the efficiency of absorbing sunlight for photosynthesis as well as warming of the surface water column, a property which determines the depth of mixing.

Under the additional assumption that the water column is vertically homogeneous over the depth where solar radiation interacts, LWLR may be interpreted using physics-based or empirical algorithms to estimate the concentration of coloured dissolved and suspended materials, including sediment and plankton. In the context of modelling studies, these biogeochemically relevant variables correspond to state variables in biogeochemical models, providing an opportunity for data assimilation in the observed surface layer. In the context of water management, the abundance of phytoplankton is key to preserving good water quality status, and turbidity may be used alongside bathymetry to determine the extent of benthic habitats, for example.

LWLR processing inherits the *Calimnos* processing chain initially developed for the UK-based GloboLakes project, in turn based on the first global inland waterbodies processing chain using a comprehensive library of algorithms and resultant products in the ESA Diversity-2 project. These processing chains were built to process archived ENVISAT-MERIS data at full resolution (300m).

Calimnos has seen continuous development in H2020 TAPAS, H2020 EOMORES, the Copernicus Land Monitoring Services (CLMS) and Lakes_cci, from core collaborative efforts between PML, University of Stirling, Brockmann Consult and HYGEOS. It is presently used to deliver the *CLMS – Lake water quality* products (LWLR, Turbidity, Trophic State Index) at 10-day aggregation intervals. For CLMS, archived MERIS full resolution data are available from *Calimnos* v1.1 whereas operational processing of Sentinel-3 OLCI uses *Calimnos* v1.2-v1.4 and Sentinel-2 MSI scenes are being processed for selected regions using *Calimnos* v1.5. The incremental versions represent evolutions of the process chain to handle newly introduced satellites, as well as updated dependencies such as POLYMER for atmospheric correction or Idepix for land/cloud/water masking. The v1.5 evolution for the MSI sensor saw algorithm adjustments to calibrate MSI products against OLCI, whilst in the Lakes_cci support for MODIS-Aqua was added with v1.5.

Lakes_cci has introduced per-pixel product uncertainty estimates and algorithms for LWLR and chlorophyll-a for MODIS-Aqua. Extension of the data record to SeaWiFs has lower priority and is not yet discussed in this document.

It should be noted that *Calimnos* is a processing chain with many processing stages, each of which are described in documents referred to in the following sections as relevant. The algorithms that form the core of atmospheric correction and retrieval of water column optical properties are all based in published literature whereas algorithm-specific tuning and their assignment to specific optical water types is unique to *Calimnos* and first described in Liu et al. (2021). The algorithm basis described here is equivalent to the ATBD provided for CLMS, with algorithm evolution and new elements for lakes cci specified in additional detail.

5.2 Algorithm definition

Calimnos combines data discovery, subsetting by target area (individual water bodies), radiometric and atmospheric corrections, pixel identification (land/cloud/water/ice), optical water type classification, individual algorithms (per parameter and water type), algorithm blending, conversion and aggregation into a single processing chain. The processes are run exclusively with optical imagery using visible and near infrared wavebands, and short-wave infrared where available.

A schematic overview of *Calimnos* is given in **Erreur ! Source du renvoi introuvable.**. The main processing stages and their corresponding algorithms are given below.

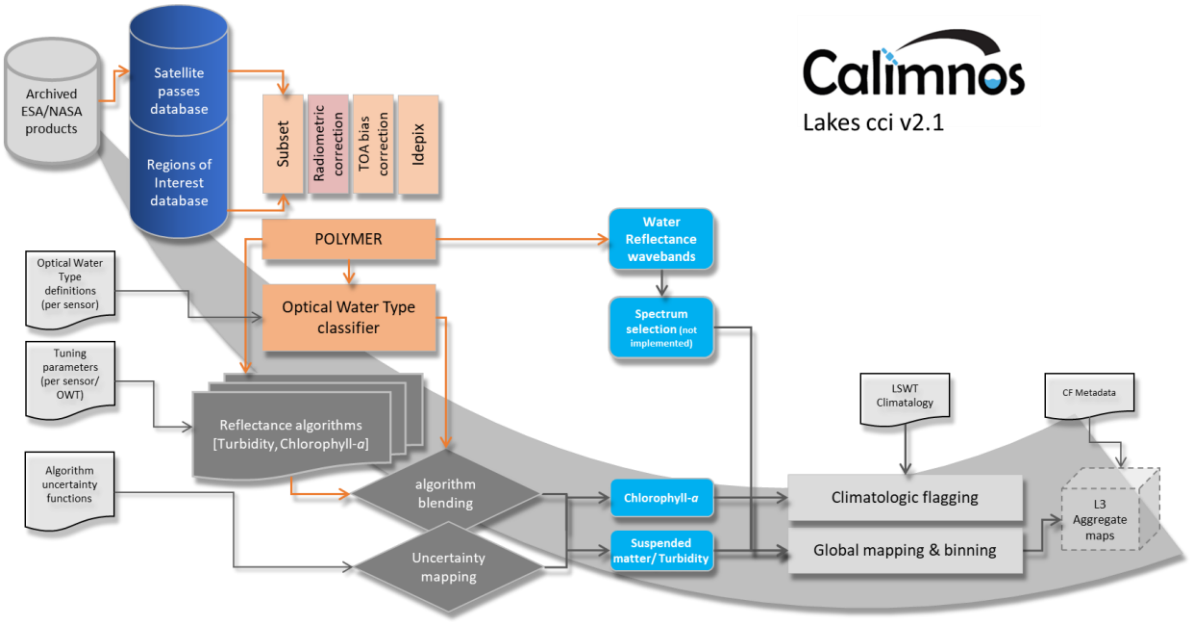

Figure 5: Schematic overview of the Calimnos processing chain for LWLR, chlorophyll-a and turbidity or suspended matter. Note that the spectrum selection step is not yet implemented and expected earliest in CRDP v3.0.

To produce Lake Water-Leaving Reflectance:

- Data discovery. Following download of new satellite passes at L1B these are entered into a geospatial database. Target regions are similarly specified in a geospatial database and satellite products which overlap any of the target regions are queued for processing. In the context of re-processing, any duplicate passes are removed. The procedure relies on in-house python scripts and postgres database functionality.
- Subsetting. For best processing performance, satellite passes are subset to bounding boxes around each target area. The subsetting routine is part of the SNAP toolbox, called through the Graph Processing Tool (GPT).
- Radiometric corrections. Any radiometric corrections defined following the release of the data are applied to the L1B imagery before submitting the data to atmospheric correction. This applies to MERIS 3rd reprocessing, using radiometric corrections as part of the SNAP toolboxes called through GPT. The 4th reprocessing of MERIS, and further radiometric corrections established for OLCI, will be used from CRDP v3.0 onwards.
- Pixel identification. The *Idepix* neural network routine is applied for initial pixel identification as water, land, cloud/haze, or snow/ice. *Idepix* is called through SNAP using the GPT. Pixel identification masks are stored for later masking of invalid (non-water) pixels.

- Atmospheric correction. POLYMER is applied to the corrected L1B data of MERIS, MODIS-Aqua and OLCI sensors and yields water-leaving reflectance wavebands. The outputs are fully normalized water-leaving reflectance per waveband. POLYMER is called using a function wrapper in Python. POLYMER was adopted from individual round-robin assessments of MERIS and MODIS, for its statistically robust retrieval of R_w with respect to linearity, relative errors, and the number of valid retrievals.

To produce derived water-column properties (turbidity and concentrations of chlorophyll-a as well as other water constituents once these reach methodological maturity):

- Optical water type classification. The optical water type (OWT) classification developed in the GloboLakes project (Spyrakos et al. 2018) is applied to each pixel to determine the similarity of the observed water-leaving reflectance spectrum to thirteen known types. The same set of OWTs is used with MERIS/OLCI and MODIS wavebands. From CRDP v2.1 onwards, additional mixed-water types are added to identify interference from adjacent land (Jiang et al. 2023).
- Algorithm mapping and blending. For each of the 13 base OWTs a best-performing algorithm (see section 5.2.2) has been selected and tuned against the global in situ reference LIMNADES data set. Algorithms for MERIS and OLCI were tuned against the whole in situ reference data set available during the GloboLakes project. For MODIS, the best-performing algorithms were selected based on atmospherically corrected satellite data, using subsets of the dataset with relatively high OWT membership scores to perform algorithm tuning per OWT (the 40 % most-similar LWLR data points were used for Chla and the top 70 % for TSM (as proxy for turbidity)). Insofar as bias correction has not already been corrected within the top-of-atmosphere product (see radiometric correction above), this step includes further corrections per algorithm, optical water type and sensor. Where no suitable algorithm/OWT combination is found, no algorithm is assigned and reported values are either missing or derived from the OWT class membership fraction for which algorithms were available. For MODIS-Aqua, no suitable TSM algorithms were found. We expect a retuning of MERIS/OLCI algorithms to follow this same procedure in preparation for v3.0 of the Lakes_cci dataset.

For uncertainty characterization:

- Uncertainty mapping. The uncertainty mapper uses results from in situ validation, separated by OWT, to produce bias and root-mean-square uncertainties per pixel. A predetermined set of uncertainty functions expresses, per output product (LWLR or derived water constituent concentrations), any non-linearity in product uncertainty as a function of (for the time being) optical water type membership.

For merged lakes (L3S) ECV product format consistency:

- Aggregation. Aggregation is done on a per-lake basis using all imagery available on a given day, after applying masks to select data for water pixels. When multiple LWLR products are available for a given day, preference is given to the MERIS or OLCI derived cloud-free results. i.e. MODIS spectra are not used. The aggregated products which contain the LWLR, chlorophyll-a and turbidity variables are then mapped to a global grid according to Lakes_cci specifications. In future versions, observations closest to solar noon will be selected instead of averaging multiple observations on the same day. This mostly affects high-latitude areas.
- Mosaicking. For consistency with other thematic lakes cci variables, the products are combined on a global grid extending from -180 to 180° longitude and -90 to 90° latitude.

Lakes selection

- All lakes_cci targets for which data is retrieved with MERIS or OLCI are included in the dataset. MODIS-Aqua data are included only for water bodies where temporal consistency

checks do not show a sensor-specific response. Typically, these are large lakes which are less subject to land adjacencies.

Climatologic filtering

From CRDP v2.1, an essential climatologic filtering procedure is implemented during the L3 reprojection and aggregation phase, to improve consistency with the LWST and LIC products. This procedure focusses on identifying unrealistic LWLR retrieval co-occurring with (sub-pixel or thin) ice cover. The climatologic filtering procedure consists of two steps, the first clustering the per-lake water quality products derived from LWLR against LWST to identify specific outliers patterns, the second to assign per-pixel quality flags based on the data distributions derived from the former step.

In the clustering step, extractions of the lake-median value for Chla, Turbidity, and LSWT are generated for each lake, for each sensor period. The LWST is a climatology calculated from daily data, spanning the 2002 - 2020 period. To determine the consistency between the water quality product and LSWT for each lake, a BIRCH clustering technique (implemented as sklearn. cluster. Birch in Python) is applied to each combination of WQ (either Chla or Turbidity) and LSWT. This process classifies the per-lake time-series into several clusters, with each cluster corresponding to different degrees of consistency between the WQ variable and LSWT. Clusters with the highest median values, lowest associated temperature, and rare occurrence are scored accordingly (Figure 6) to determine whether they are likely good, low or poor quality observations.

In the second step, data distributions of WQ and LSWT for each cluster are used to assign per-pixel good, poor and low consistency flags to the L3 products. Any observations where the LSWT climatology is > 278K remains categorized as good. For the remaining observations, a decision tree (Figure 7) is used.

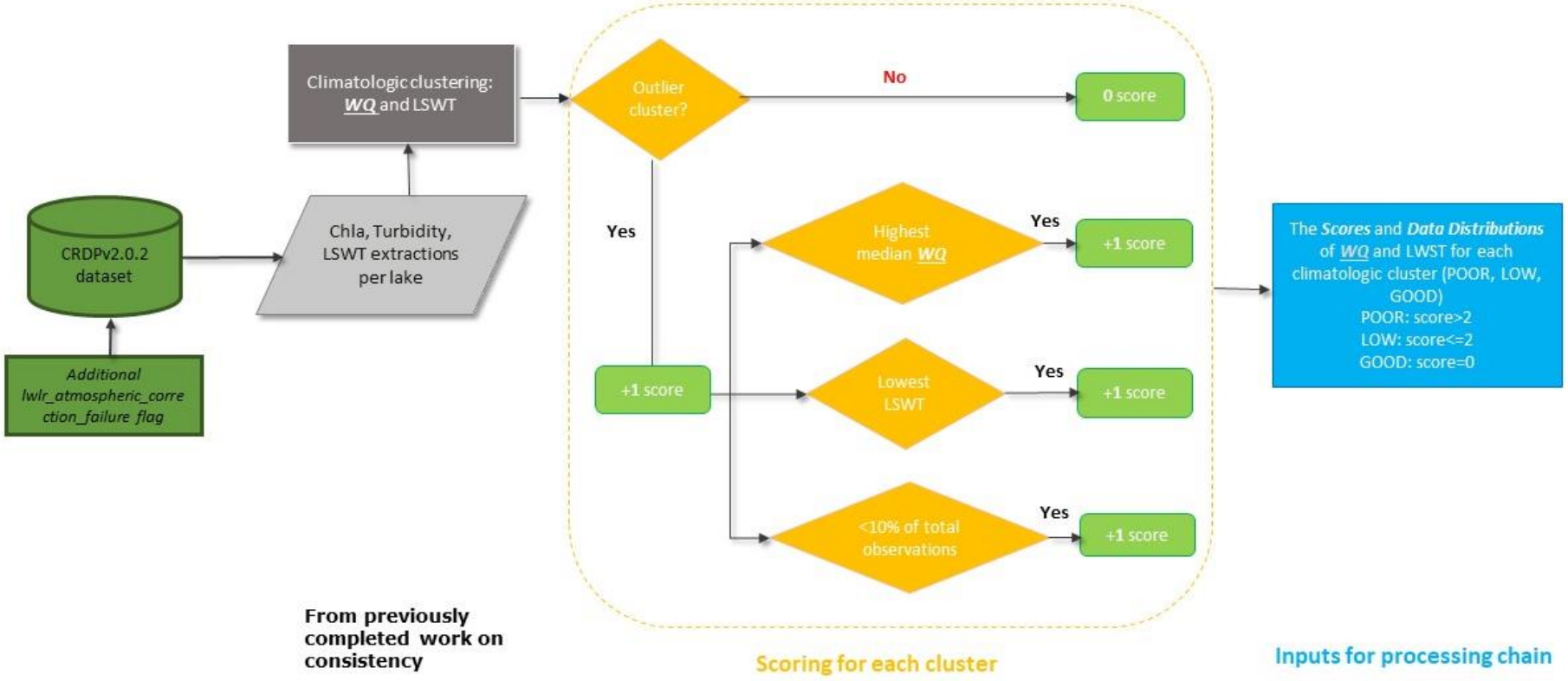

Figure 6 Climatologic clusters generation and the scoring system.

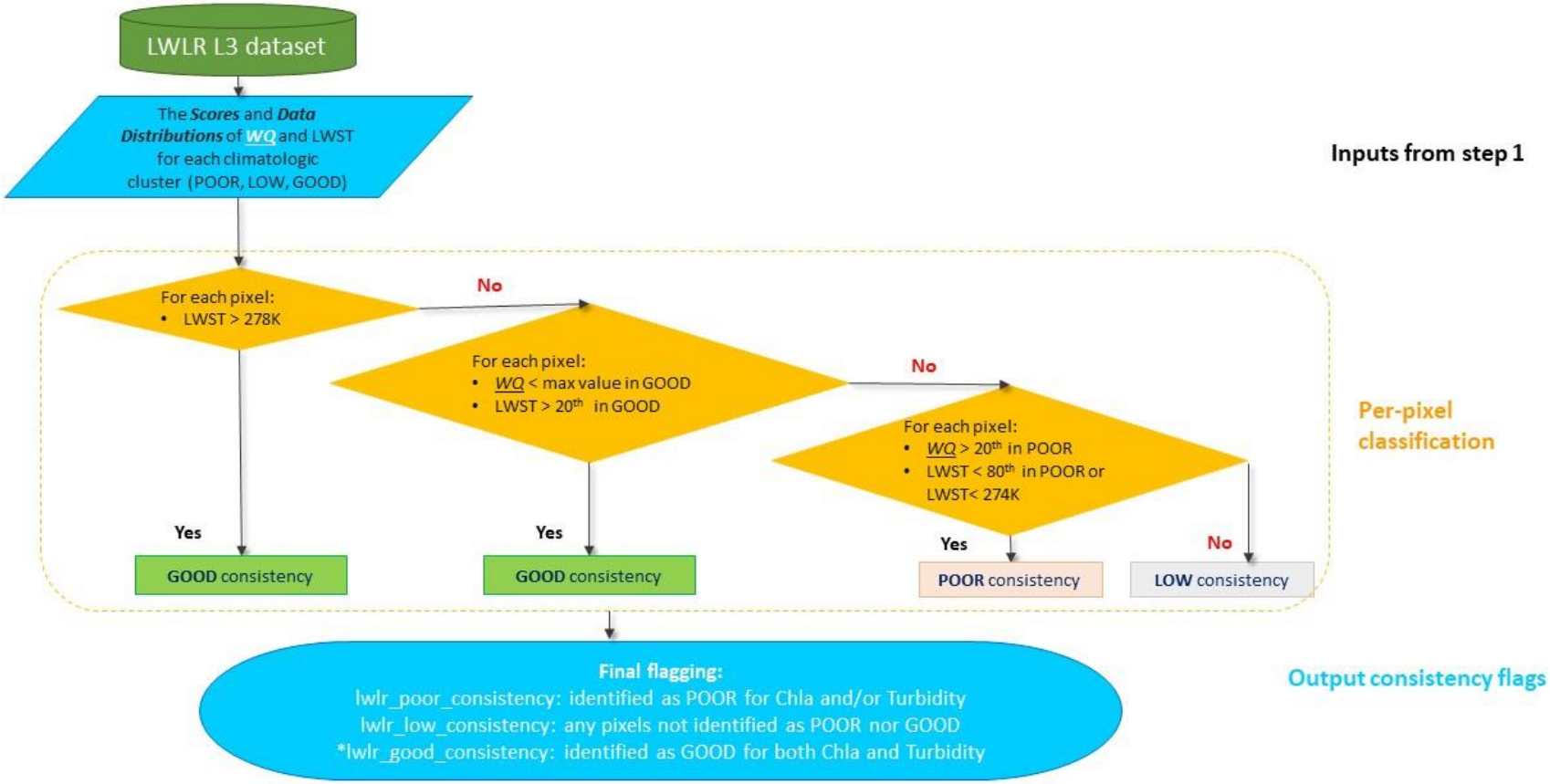

Figure 7 Climatologic consistency flags generation.

The lwlr_quality_flag band in CRDP v2.1 provides essential information to users regarding the reasons behind missing observations and aids in the proper utilization of the data. Apart from the two flags generated by the climatologic filtering procedure, there are six additional flags included in the lwlr_quality_flag band. The complete list of quality flags incorporated in the lwlr_quality_flag band is as follows:

- lwlr_cloud: not processed due to suspected cloud
- lwlr_land: not processed due to suspected land
- lwlr_snow_ice: not processed due to suspected snow or ice
- lwlr_bright_pixel: masked due to extreme reflectance values
- lwlr_land_contaminated: risk of land influence on water signal
- lwlr_atmospheric_correction_failure: no atmospheric correction result
- lwlr_poor_consistency: illegal combination of LWLR, LWST, and/or LIC
- lwlr_ low_consistency: pixel includes at least some suspect combinations of LWLR, LWST, and/or LIC

5.2.1 Algorithm assumptions and known limitations

The following assumptions relating to individual algorithms are core to the performance of the processing chain for LWLR and derived substance concentrations:

- *Idepix* can differentiate adequately between pixels containing water and any of the following conditions: mixed land/water, cloud, cloud shadow, ice, snow, and haze.
- *POLYMER* successfully retains the shape and amplitude of water-leaving reflectance.
- The Optical Water Type classification sufficiently captures the diversity of natural water types so that the most appropriate algorithms can be used and tuned to remove systematic bias.
- Tuning of reflectance algorithms for chlorophyll-*a* and turbidity is adequate for each water type and based on sufficient in situ data availability to achieve statistical rigour.

5.2.2 Specific algorithms for LWLR

5.2.2.1 Pixel geolocation

The standard MERIS 3rd reprocessing needs a geometric correction step which is performed by the AMORGOS software developed by ACRI-ST and provided by ESA (see earth.esa.int/services/amorgos/download/Amorgos_ICD-SUM_3.0a.pdf and earth.esa.int/services/amorgos/download/Amorgos_STD_i3r0p1.pdf). It includes a precise orbit determination, instrument pointing and performs an ortho-rectification. The improvement in the geolocation is documented in Bicheron et al. (2011). For *Calimnos,* AMORGOS geometrically corrected lat/lon bands are archived alongside the original L1B product, used to identify the area to be processed and patched in at the end of L2 processing. The resulting accuracy is improved by Amorgos and is specified in Bicheron et al. (2011) as better than 70m for MERIS FR pixels.

For OLCI, no further processing step for improving the geolocation position is required. The accuracy is given by ESA with 0.2 – 0.7 pixels for processing version 2.23 and <0.1 pixel for processing version 2.29.

For MODIS Aqua, a GEO file is generated based on satellite attitude and ephemeris data provided by NASA, to produce L1C data as input to further processing.

5.2.2.2 Radiometric corrections

OLCI-A is the reference system for inter-sensor bias corrections, because it has the largest number of spectral bands and benefits from a larger vicarious calibration network than any earlier sensor. A per-band system vicarious gain correction is currently available for use with POLYMER.

For MERIS, the coherent noise equalization method reduces detector-to-detector and camera-to-camera systematic radiometric differences and results into a diminution of the vertical stripping observed on MERIS L1b products following the algorithm developed by Bouvet and Ramino (2010); coefficients for each detector line are retrieved from MERIS archive over ice. Another step for radiometric improvements is the smile correction, which corrects for the small variations of the spectral wavelength of each pixel along the image by the estimation of the reflectance spectral slope from the measurements in two neighbouring bands. POLYMER uses actual pixel wavelength, so smile correction is not used in this processing chain.

For MERIS and MODIS, sensor-specific bias corrections, including any known system vicarious calibration gains, are applied within the POLYMER atmospheric correction step.

5.2.2.3 Pixel identification

The cloud detection function of the Idepix algorithm developed by Brockmann Consult was used in several processing chains, e.g. those used in CoastColour L1P and Diversity II. Meanwhile, many steps of the Idepix algorithm are included in the upcoming MERIS 4th reprocessing as standard algorithm by ESA. Due to the good performance of Idepix cloud screening in these applications, it is also selected for *Calimnos*. Idepix is based on a cloud probability derived from a neural net which has been trained with >60,000 manually classified pixels and which is combined with a number of additional tests on e. g. brightness, whiteness, glint. After clouds have been identified, a buffer can be defined in order to provide for a safety margin along cloud borders. This buffer radius (in pixel) can be parameterized and is set to 2 pixels.

Validation is performed by applying the PixBox Validation, a procedure where manually selected pixels are categorized to different categories and characterized with expert knowledge, e. g. to clear land, clear water, totally cloudy, semi-transparent cloud, cloud shadow, snow/ice, etc. A set of 17k MERIS FR pixels was collected in the scope of the CoastColour project, and detailed validation results are provided in the corresponding report (Ruescas et al. 2014).

Retrieval of water quality parameters is also strongly influenced by the occurrence of cloud shadow, which need to be identified and eliminated from further processing. Potential cloud shadow areas are identified by the geometry of the sun angle, viewing angle and the cloud height and the cloud bottom. The cloud height is gained by either the pressure or the temperature, but if this information is missing (not all sensors offer the respective bands), a maximum cloud height needs to be defined. The most difficult prediction is the height of the cloud base as it is not seen by the sensor. In Idepix it is defined as the minimum cloud height detected within the respective cloud minus an offset. Basis of good cloud shadow detection is a good cloud detection. Validation of the cloud shadow detection is done by visual inspection of different images under different conditions (cloud types and geometries).

In general, the most progressive combination of available cloud masks is selected, favouring accuracy over observation coverage.

5.2.2.4 Atmospheric correction

POLYMER versions 4.12-14 (having equivalent outputs for the sensors used here) were used to produce CRDP v2.0.2 and its temporal extension v2.1. The atmospheric correction processor was initially designed to resolve water-leaving reflectance in clear ocean waters including areas affected by sun glint (Steinmetz et al. 2011). The versatility of the processor to deal with bright waters has tested positively with a variety of optically complex (including inland) waters compared to alternative processors (Qin et al. 2017, Warren et al. 2019), although systematic under-estimation of reflectance in turbid and productive waters is evident. POLYMER applies a spectral optimization based on bio-optical model in conjunction with radiative transfer models to separate atmospheric (including glint) and water reflectance. The principle of the algorithm is a spectral matching method using a polynomial to model the spectral reflectance of the atmosphere and sun glint, and a bio-optical forward reflectance model for the water part. The algorithm uses the full set of wavebands available (user-configurable) as opposed to alternative ocean-colour methods that primarily extrapolate from near infra-red bands. The output are fully normalized water-leaving reflectances.

Configuration:

- POLYMER according to Steinmetz et al. (2011), updated in Steinmetz (2016 and 2018), parameterized to use the Park and Ruddick (2005) bidirectional reflectance distribution function and operating only on pixels identified as water by the *Idepix* module (masks generated by POLYMER are not used). Starting conditions for the optimization procedure are set to chlorophyll-a = 1 mg m^{-3} and the scattering coefficient f_b = 1 and bounds for these variables are widened to 0.01 – 1000 mg m^{-3} Chl-a and -3 to 3, respectively.

5.2.2.5 Specific algorithms for derived water quality products

5.2.2.5.1 Optical water type (OWT) membership

The OWT classification module was written at PML based on the work of Moore et al. (2001) and equivalent software developed for ESA Ocean Colour cci. The algorithm used for lakes relies on a spectral library (spectral means) defined in the GloboLakes project by the University of Stirling (Spyrakos et al. 2018). In contrast to OWT mapping used in earlier versions of *Calimnos*, CLMS and Lakes_cci adopt the spectral angle (Kruse et al. 1993) rather than Mahalonobis distance as metric for similarity between observations and type spectra. The spectral angle is here defined over a range of 0 to 1 where 1 implies identical spectra.

5.2.2.5.2 Water constituent algorithms

Weighted blending: Water constituent retrieval algorithms tuned to each OWT (Spyrakos et al. 2018, Neil et al. 2019) are mapped to individual pixels from the OWTs with the three highest classification scores for that pixel. The algorithm results corresponding to those three OWTs are averaged using the membership score as weighting factor, after normalizing the scores between 0 and 1 where 1 is the highest score and 0 is the score of the 4th ranking OWT. This procedure is used to derive maps of total suspended matter (TSM) and chlorophyll-*a* (Chla) without discontinuities at the edge of the applicable range of any single algorithm.

Uncertainty mapping: to propagate product uncertainty from the individual algorithms, the weighted OWT membership score is again used, in combination with a set of uncertainty functions resulting from in situ algorithm validation. The uncertainty functions describe product uncertainty as a function of OWT membership score and target substance concentration (where relevant). The per-OWT uncertainties are weighted according to OWT-membership to allow propagation to the final product. Where in situ data are lacking in lakes to determine product uncertainties (e.g. in the case

of a specific OWT, substance concentration range or sensors), and uncertainty cannot be provided this value is set to Inf (infinity).

5.2.2.5.3 Chlorophyll-a algorithms

5.2.2.5.3.1 Chlorophyll-a algorithms for MERIS

Table 4 lists the mapping of algorithms to specific OWTs as given in Spyrakos et al. (2018). Each algorithm is tuned to one or more OWTs, depending on their published range of applicability and the wavebands used in their design. The algorithms set out below are those selected for MERIS after extensive product validation in the GloboLakes project (Neil et al. 2019). It is noted that while the methodology of algorithm tuning is as described in Neil et al. (2019), tuned algorithm coefficients may differ since the former are derived from calibration of in situ reflectance data against LIMNADES whereas *Calimnos* uses coefficients optimised for POLYMER-corrected normalized water-leaving reflectance. OLCI offers the same set of wavebands as MERIS, but validation of OLCI-specific algorithms is limited by scarce in situ data availability. For OLCI, therefore, we adopt the MERIS configuration of algorithms which may be further adjusted following consistency checks (preliminary analysis within CLMS suggests that no adjustment is required).

Table 4: Chlorophyll-a algorithms per optical water type for MERIS

Optical water type number	Algorithm source	Algorithm optimization
3, 9, 10, 13	OC2 oceancolor.gsfc.nasa.gov/cms/atbd/chlor_a	Empirical re-tuning of algorithm parameters based on GloboLakes calibration against the Limnades database, specific to each optical water type (Neil et al. 2019).
2, 8, 11, 12	708/665 empirical band ratio based on Gilerson et al. (2010)	
1, 4, 5, 6	Semi-analytical NIR-Red band algorithm for MERIS based on Gons et al. 2005.	
7	Adapted QAA algorithm according to Mishra et al. (2013)	

Selected algorithm parameters for each of the four options were tuned in GloboLakes against the LIMNADES database to accommodate for variability in retrieval accuracy over the range of inland waters encountered in the LIMNADES dataset. This procedure also accounts for any uncertainties that stem from systematic bias in the retrieval of water-leaving reflectance from POLYMER. This whole-chain validation is applied to each algorithm in *Calimnos*, recognizing the fact that the most prominent error in inland water quality retrieval is the atmospheric correction step. It is noted that validation data for relatively clear inland waters are very scarce.

The OC2 algorithm, originally formulated to retrieve chlorophyll-a concentration from relatively clear ocean waters where phytoplankton and other optically active substances covary, relies on a ratio of blue and green wavebands. The algorithm is formulated as:

$$log(Chla) = a_0 + (a_1 x) + a_2 x^2 + a_3 x^3 + a_4 x^4 \qquad [5.1]$$

where x is the reflectance band ratio:

$$x = log\ \frac{R_w(490)}{R_w(560)}. \qquad [5.2]$$

The tuned algorithm coefficients used in Calimnos are a_0 = 0.1731, a_1 = -3.9630, a_2 = -0.5620, a_3 = 4.5008 and a_4 = -3.0020. R_w is the fully normalized water-leaving reflectance.

The remaining three algorithms are variations on empirical and semi-analytical retrieval methods that focus on interpreting the red to near-infrared part of the spectrum. These methods are the most successful approach to retrieve chlorophyll-a concentration over a range of turbidity and trophic levels, because the red part of the spectrum is least influenced by overlapping absorption signatures of dissolved substances and other phytoplankton pigments.

The Gilerson et al. (2010) algorithm is an empirically tuned ratio of bands 708 and 665 nm. The tuning of the algorithm is revised in *Calimnos*, by calibrating against the LIMNADES data set (for OWTs 2, 8, 11, and 12) which is much larger than the data set used in the original publication (Neil et al. 2019). The final configuration is a highly simplified form of the original algorithm:

$$Chla\ [mg\ m^{-3}] = A \times \left(\frac{R(709)}{R(665)}\right)^{B} + C \qquad [5.3]$$

Where A = 76.62, B = 0.7393 and C = -54.99 are tuning coefficients empirically calibrated against LIMNADES. $R(\lambda)$ is the reflectance (irrespective of whether it is expressed above or below water and normalized for viewing geometry or not) at waveband λ.

The Gons et al. (2005) algorithm (tuned to OWTs 1, 4, 5, 6) uses the same band ratio and additionally analytically retrieves the backscattering coefficient from the 778 nm band. Subsequently the absorption at 665 nm is analytically retrieved by inverting the Gordon reflectance model and attributed to chlorophyll-*a* and water. Empirical tuning is restricted to the slope of the backscattering coefficient and a chlorophyll-*a* specific absorption coefficient determined from eutrophic inland waters. The algorithm is thus specified as follows:

$$Chla\ [mg\ m^{-3}] = \left[\left(\frac{R(709)}{R(665)}\right) \times (a_w(709) + b_b) - a_w(665) - b_b^P\right] / a^*_{chl}(665) \qquad [5.4]$$

Where $a_w(709)$=0. 84784 m^{-1} and $a_w(665)$=0. 431138 m^{-1} represent the absorption by pure water from Roettgers et al. (2011). Further, $a^*_{chl}(665)$ = 0. 025 $m^2\ mg^{-1}$ is the chlorophyll-a specific absorption coefficient following calibration against LIMNADES. The empirical constant P=1. 06 was not changed from the original formulation. The backscattering coefficient b_b is considered spectrally neutral and derived from a single near infra-red waveband:

$$b_b = \frac{0.6 \times a_w(779) \times R_w(779)}{0.082 - 0.6 \times R_w(779)} \qquad [5.5]$$

The Mishra et al. (2013) implementation of the Quasi-Analytical Approach (QAA) is similar to the analytical inversion of Gons et al. (2005) but with a slightly different set of input bands and subsequent tuning parameters. In *Calimnos* it is exclusively mapped to OWT 7. The QAA chlorophyll-a product is derived from the phytoplankton absorption at 665nm, empirically tuned against LIMNADES as follows:

$$Chla\ [mg\ m^{-3}] = A \times a_{ph}(665)^{B} \qquad [5.6]$$

Where A = 63. 375 and B = 0. 442. The $a_{ph}(665)$ is retrieved from a set of equations, accounting for non-phytoplankton absorption in this band through the interpretation of absorption in blue and green wavebands:

$$a_{ph}(665) = a(665) - a_w(665) - a_{ys}(665),$$

$$a_{ys}(665) = a_{ys}(442)e^{-S(665-442)},$$

$$a_{ys}(442) = \frac{(a(412) - s_1 \times a(442)) - (a_w(412) - (e_1 \times a_w(412)))}{e_1 - s_1} \quad [5.7]$$

where the absorption by water a_w is again obtained from Roettgers et al. (2011), S = 0.0135 nm^{-1} is the average exponential slope coefficient for yellow substances derived from LIMNADES, and e_1 and s_1 are defined as

$$s_1 = 0.74 + \frac{0.2}{0.8 + \frac{rrs(442)}{rrs(560)}},$$

$$e_1 = e^{S(442-412)} \quad [5.8]$$

where the absorption in bands 412, 442 and 665 nm is obtained as

$$a(\lambda) = \frac{(1.0 - u(\lambda)) \times (b_{bw}(\lambda) + b_b(\lambda))}{u(\lambda)}. \quad [5.9]$$

Here, $b_{bw}(\lambda)$ is the backscattering coefficient of pure water obtained from Morel (1974) assuming zero salinity. In turn, $u(\lambda)$is the ratio of backscattering to the sum of backscattering and absorption, which according to the work by Gordon et al. (1988) can be obtained from below-surface remote-sensing reflectance $rrs(\lambda)$ as:

$$u(\lambda) = \frac{-g_0 + \sqrt{g^2 + (4 \times g_1) \times rrs(\lambda)}}{2 \times g_1}, \quad [5.10]$$

With g_0 = 0.089 and g_1 = 0.125. The *rrs* bands are obtained from the LWLR (which corresponds to fully normalized water-leaving reflectance, $R_w(\lambda)$) using:

$$rrs(\lambda) = \frac{R_w(\lambda)}{\pi(0.52 + 0.54 \times R_w(\lambda))} \quad [5.11]$$

5.2.2.5.3.2 Chla algorithms for MODIS

For MODIS-Aqua, each selected algorithm was tuned to each OWT for the optimal assignment of algorithms as shown in Table 5. Only matchups with the top-40% of OWT membership scores were used for the tuning of these algorithms. This is done to improve the overall performance of Chla algorithms across diverse optical properties as well as assess the appropriate algorithms and parameterizations for given scenarios, which means although assigned to the same algorithm, different OWTs would adopt different tuned parameterizations. The algorithm selection and assignment presented here is based on matchups between in situ and POLYMER-corrected MODIS Rw in LIMNADES.

Table 5: Chlorophyll-a algorithms per optical water type for MODIS

Optical water type number	Algorithm source	Algorithm optimization
1, 5, 7, 9, 12,13	OC2 oceancolor.gsfc.nasa.gov/cms/atbd/chlor_a	Empirical re-tuning of algorithm parameters based on GloboLakes calibration against the Limnades database, specific to each optical water type. (analogous to Neil et al. 2019 for chlorophyll-*a*).
2, 3, 8	OC3 oceancolor.gsfc.nasa.gov/cms/atbd/chlor_a	
4, 6, 11	748/667 empirical band ratio based on Gilerson et al. (2010)	
10	OC2_HI oceancolor.gsfc.nasa.gov/cms/atbd/chlor_a	

The OCX algorithms, originally formulated to retrieve chlorophyll-a concentration from relatively clear ocean waters where phytoplankton and other optically active substances covary, relies on a ratio of blue and green wavebands. The algorithm is formulated as:

$$log(Chla) = a_0 + (a_1 x) + a_2 x^2 + a_3 x^3 + a_4 x^4 \quad [5.12]$$

For OC2, where x is the reflectance band ratio:

$$x = log \frac{R_w(490)}{R_w(560)}. \quad [5.13]$$

For OC3, where x is the reflectance band ratio:

$$x = log \frac{min\,(R_w(443), R_w(490))}{R_w(560)} \quad [5.14]$$

For OC2_HI, where x is the reflectance band ratio:

$$x = log \frac{R_w(469)}{R_w(560)}. \quad [5.15]$$

R_w is the fully normalized water-leaving reflectance. The tuned algorithm coefficients of OCX algorithms for each OWT are listed in Table 6.

Table 6: Coefficients of OCX algorithms for each assigned OWT

Algorithm	OWT	a0	a1	a2	a3	a4
OC2	1	0.2750	-2.7227	1.5467	-3.1056	0.5945
OC2	5	0.2875	-2.8465	1.6170	-3.2468	0.6216
OC2	7	0.2750	-2.7227	1.5467	-3.1056	0.5946
OC2	9	0.2875	-2.7419	1.3401	-2.5856	0.5996
OC2	12	0.2750	-2.7227	1.5467	-3.0026	0.4918
OC2	13	0.2731	-2.7227	1.5467	-2.7567	0.4865
OC3	2	0.3030	-3.4279	1.8476	0.001875	-1.5350
OC3	3	0.1939	-3.0978	1.8570	0.00120	-1.2255
OC3	8	0.2665	-3.0165	1.9582	0.001382	-1.2897
OC2_HI	10	0.1171	-2.1544	1.1662	-0.9983	-0.6458

The Gilerson et al. (2010) algorithm for MODIS is an empirically tuned ratio of bands 748 and 667 nm. The final configuration is a highly simplified form of the original algorithm:

$$Chla\ [mg\ m^{-3}] = A \times \left(\frac{R(748)}{R(667)}\right)^B + C \quad [5.16]$$

Where the optimized empirical coefficients calibrated against LIMNADES for OWTs 4, 6 and 11 are:

A4=2.008, B4=1.656, C4=-2.035; A6=2.0, B6=1.587, C6=-2.954; A11=2.149, B11=1.519, C11=-6.447. $R(\lambda)$ is the reflectance (irrespective of whether it is expressed above or below water and normalized for viewing geometry or not) at waveband λ.

5.2.2.5.4 Turbidity and suspended matter algorithms

Turbidity and total suspended matter (TSM) may be retrieved from LWLR in wavebands where phytoplankton and dissolved organic matter absorption do not significantly influence the amplitude of the reflectance. Ultimately, turbidity and suspended matter algorithms are empirically related to the efficiency of light backscattering compared to absorption. The absorption of light becomes increasingly predictable with waveband due to the efficiency of absorption by pure water at longer wavelengths. Candidate algorithms to directly convert the signal to either Turbidity or suspended matter dry weight, using a conversion factor of 1.17 NTU/g m^{-3} between suspended matter and Turbidity, have been formulated by Nechad et al. (2010, 2016). This conversion factor is currently used in *Calimnos* to obtain Turbidity from several suspended matter retrieval algorithms, pending validation of which algorithms perform better over specific optical water types.

5.2.2.5.4.1 TSM algorithms for MERIS

The suspended matter algorithms for MERIS selected per Optical Water Type as shown in Table 7.

Table 7: Suspended matter algorithms per optical water type for MERIS

Optical water type number	Algorithm source	Algorithm optimization
1, 7, 10	Based on Zhang et al. (2014)	Empirical re-tuning of algorithm parameters based on GloboLakes calibration against the Limnades database, specific to each optical water type (analogous to Neil et al. 2019 for chlorophyll-*a*).
2, 4, 6, 8, 12	Based on Vantrepotte et al. (2011)	
3, 5, 9, 11, 13	Based on Binding et al. (2010)	

The Binding et al. (2010) algorithm as it is implemented here is based on the analytical inversion of reflectance in the 754 nm band and converting the resultant particulate backscattering signal using a mass-specific backscattering coefficient for suspended matter:

$$TSM\ [g\ m^{-3}] = \frac{a_w(754) \times R_w(754)}{f \times B \times b^*_{TSM}} \qquad [5.17]$$

where the absorption by water $a_w(754)$ = 2. 8 m^{-1}, the backscattering-to-scattering ratio B=0. 019. The TSM-specific scattering coefficient b_{TSM}^* = 0. 664 $m^2\ g^{-1}$ and is the only coefficient that was optimized against LIMNADES.

The Vantrepotte et al. (2011) algorithm as it is implemented here is similar but uses the 665 nm band and an additional empirical factor, which is also tuned to provide the best match for the corresponding water types:

$$TSM\ [g\ m^{-3}] = \frac{A \times R_w(665)}{1 - \frac{R_w(665)}{B}} + C \qquad [5.18]$$

where the optimized empirical coefficients are A = 206.4, B = 20460.0 and C = -0.7921.

The Zhang et al. (2014) algorithm as it is implemented here is an empirical relation between the 709 nm band and in situ measured suspended matter dry weight, tuned as with the algorithms above:

$$TSM\ [g\ m^{-3}] = A \times \frac{R_w(709)^B}{\pi} \qquad [5.19]$$

where the optimized empirical coefficients are *A* = 2524.0 and *B* = 1.113.

5.2.2.5.4.1 TSM algorithms for MODIS

The TSM algorithm selection and assignment for MODIS are shown in Table 8.

Table 8: Suspended matter algorithms per optical water type for MODIS

Optical water type number	Algorithm source	Algorithm optimization
1, 12	Based on Miller and McKee (2004)	Empirical re-tuning of algorithm parameters based on GloboLakes calibration against the Limnades database, specific to each optical water type (analogous to Neil et al. 2019 for chlorophyll-*a*).
2, 6, 11, 13	Based on Ondrusek et al. (2012)	
3, 5, 9	Based on Chen et al. (2007)	
4, 8, 10	Based on Petus et al. (2010)	
7	Based on Zhang et al. (2010)	

The Miller and McKee (2004) algorithm as it is implemented here is an empirical linear relationship between the 645nm band and in situ measured suspended matter dry weight, which is tuned to provide the best match for each of the corresponding water types:

$$TSM\ [g.m^{-3}] = A \times\ R_w(645) + B \qquad [5.20]$$

where the optimized empirical coefficients for OWTs 1 and 12 are: A1=362.954, B1=-1.659; A12=362.953, B12=-1.844.

The Ondrusek et al. (2012) algorithm as it is implemented here is an empirical 3rd order polynomial relation between the 645nm band and in situ measured suspended matter dry weight, which is also tuned for each of the corresponding water types

$$TSM\ [g.m^{-3}] = A \times R_w(645)^3 +\ B \times R_w(645)^2 +\ C \times R_w(645) \qquad [5.21]$$

where the optimized empirical coefficients for OWTs 2, 6, 11, and 13 are: A2=0.156, B2=-1.821, C2=477.400; A6=0.0876, B6=-1.821, C6=243.764; A11=0.0876, B11=-1.821, C11=419.895; A13=0.0876, B13=-1.821, C13=500.

The Chen et al. (2007) algorithm as it is implemented here is an empirical power-law relation between the 645nm band and in situ measured TSM, which is tuned for each of the assigned water types:

$$TSM\ [g.m^{-3}] = A \times R_w(645)^B \qquad [5.22]$$

Where the optimized empirical coefficients for OWTs 3, 5, and 9 are: A3=1023.315, B3=1.202; A5=963.12, B5=1.204; A9=1203.900, B9=1.252.

The Petus et al. (2010) algorithm as it is implemented here is an empirical 2nd order polynomial relation between the 645nm and TSM, which is tuned to each of the assigned OWTs:

$$TSM[g.m^{-3}] = A \times R_w(645)^2 + B \times R_w(645) + C \qquad [5.23]$$

Where the tuned parameters for OWTs 4, 8, and 10 are: A4=1, B4=209.4675359, C4=2116.900; A8=1, B8=189.372, C8=2468.043; A10=0.857, B10=215.674, C10=2651.265

The Zhang et al. (2010) algorithm as it is implemented here is an empirical multi-band exponential relation between the 488nm, 555nm, 645nm, and TSM, which is tuned to OWT 7:

$$log10(TSM)[g.m^{-3}] = A + B \times \left(R_w(555) + R_w(645)\right) + C \times (R_w(488)/R_w(555)) \quad [5.24]$$

Where the tuned parameters are: A7=0.706, B7=7.078, C7=-0.583.

5.3 Input products and dependencies

Satellite input data:

- Envisat MERIS L1B at reduced resolution (3rd reprocessing, 4th Full Resolution in v3.0)
- Sentinel 3A/B OLCI L1B (SAFE format)
- MODIS Aqua L1A (+ GEO files)

Lake water boundaries:

- maximum water extent observed in ESA CCI Land Cover (v4.0) at 150-m resolution
- polygons generated (including manual inspection) at PML (doi: 10.5281/zenodo.3349547).

POLYMER ancillary data:

- ECMWF Meteorological Analysis data bundled with OLCI NTC (source ESA/EUM)
- Global Modeling and Assimilation Office (NASA GMAO) atmospheric optical data (Forward Processing)

Optical water type definitions (mean spectra standardized using Simpson's criterion)

- GloboLakes project (Spyrakos et al. 2018)
- Adjacent-land affected water types (Jiang et al. 2023)

5.4 Output product

The output data (product bands) are produced as gridded variables in a NetCDF file. Variables include each reflectance band, the derived chlorophyll-a and turbidity and the associated per-pixel uncertainty for each of these. The uncertainties for the LWLR variables are given both as relative and detrended relative uncertainties because systematic uncertainties in LWLR are assumed to be resolved in the tuning of derived biogeochemical products, thus providing more insight into the source of uncertainty. Intermediary products are not distributed but are generally stored for product validation and improvement purposes and may be requested from PML for specific studies. These include the specific outputs from individual algorithms (prior to mapping/blending) and all processor-generated flags. A detailed overview of the output bands, their data types and attributes are provided in the Product Specification Document (PSD).

5.5 Quality Assessment

Quality assessment of the LWLR and derived products is based on validation against in situ observations. This section contains an overview of product quality assessment efforts resulting from past and present validation activities, to provide the user sufficient information to determine which variables are suitable for their particular use case.

Results provided here are for in situ validation carried out against observations with the MERIS and MODIS sensors, for which by far the most in situ data are available.

5.5.1 Atmospheric correction

5.5.1.1 MERIS

The initial round-robin comparison of atmospheric correction algorithms for MERIS showed that POLYMER (v3.5) yielded the statistically most robust retrieval of R_w particularly with respect to linearity and relative errors. However, a systematic negative bias was observed in the matchup validation. Given the low number of matchups in that analysis, an expanded validation of atmospheric-corrected R_w for MERIS has been conducted with updated POLYMER (v4.12) and expanded matchup dataset (Figure 8) but with a matchup window reduced to ±3 days. Note that the new results are shown in log scale to better assess performance in the lower range. Systematic underestimation of MERIS R_w was observed for all wavebands with bias ranging from -0.008 sr^{-1} in the 779 nm to -0.030 sr^{-1} at 560 nm (Figure 8).

5.5.1.2 MODIS

The performance of POLYMER-corrected MODIS Rrs matchups was assessed with in situ Rrs at 11 bands from 412 nm to 748 nm (Figure 9). Significant linear correlations were found for all bands, with the highest R of 0.83 returned in 547 nm. A systematic underestimation was observed with Bias ranging from -0.004 sr^{-1} at 412 nm to -0.023 sr^{-1} at 555 nm.

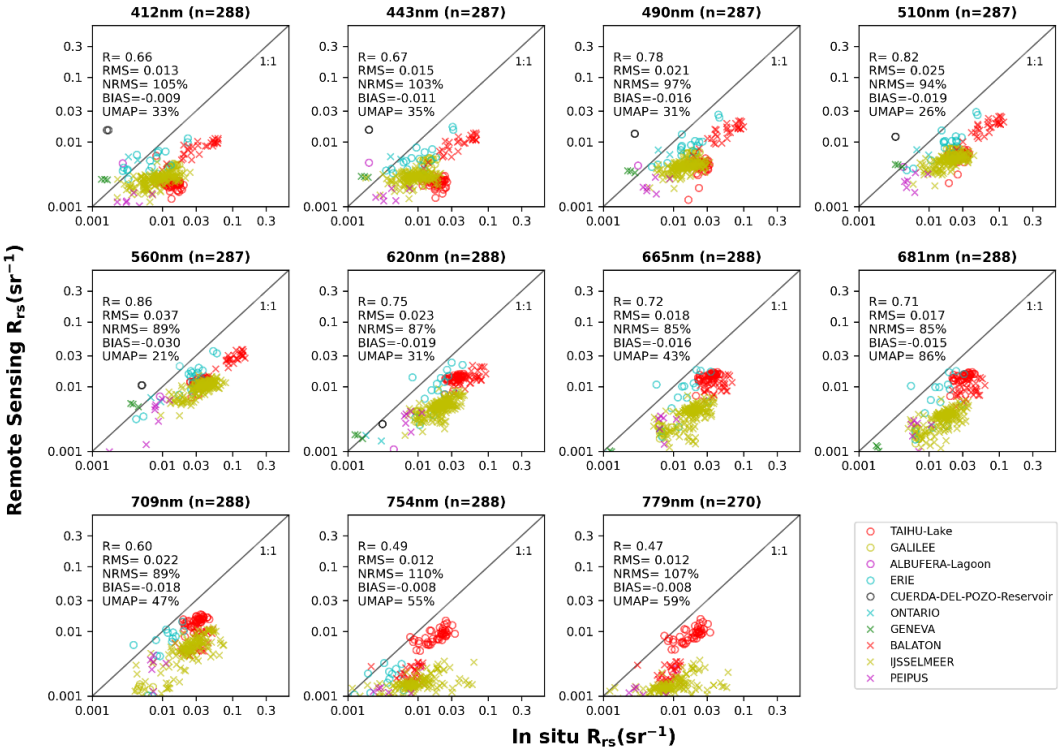

Figure 8: POLYMER v4.12 matchups of MERIS with in situ reflectance data in LIMNADES, using a ±3 day matchup window and 3x3 pixel extraction window.

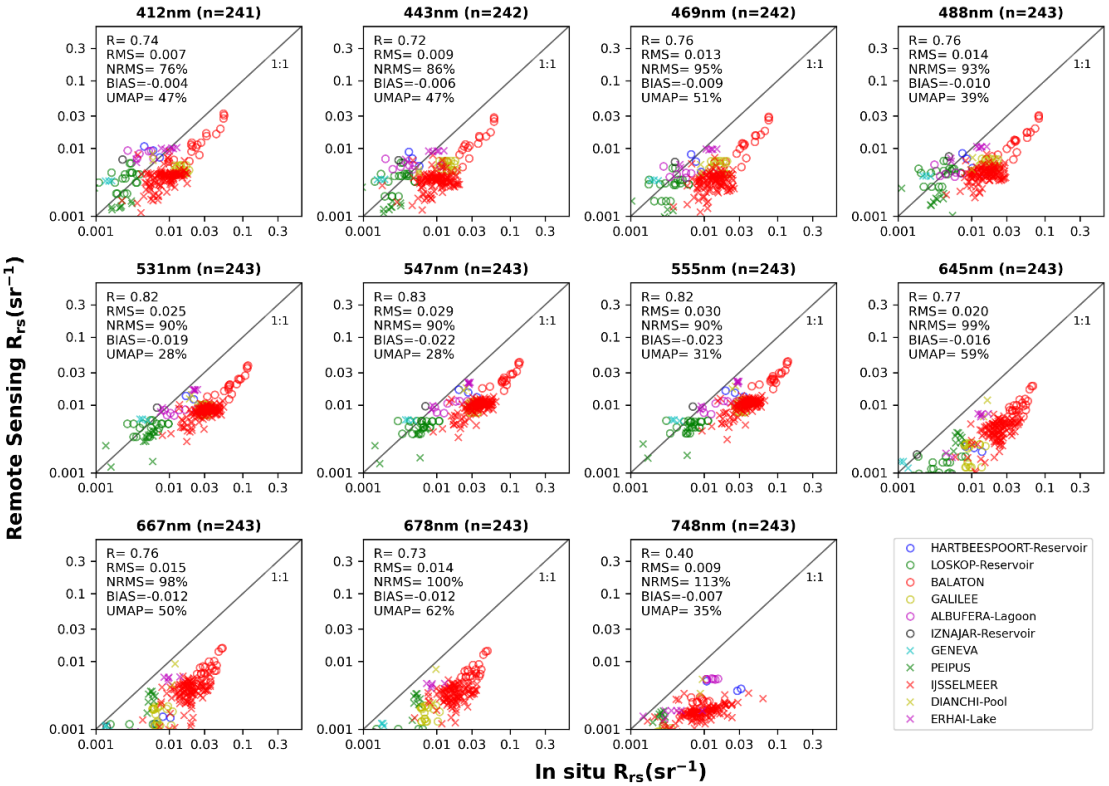

Figure 9: POLYMER v4.12 matchups of MODIS with in situ reflectance data in LIMNADES, using a ±3 day matchup window and 3x3 pixel extraction window.

5.5.2 Weighted blending of biogeochemical variable algorithms

The end-to-end calibration methodology with specific tuning of algorithms corresponding to sets of optical water types is believed to counteract the systematic bias in LWLR retrieval. Furthermore, the number of matchup data points for validation of chlorophyll-a and turbidity or suspended matter is much higher.

Neil et al. (2019) presented the results of algorithm calibration using exclusively in situ radiometry and substance concentrations determined from water samples. During GloboLakes, further tuning of the algorithms was carried out to calibrate the algorithms against atmospherically corrected satellite data (using POLYMER and other candidate atmospheric correction algorithms for MERIS).

Results shown below are from a recent uncertainty characterization analysis of the chlorophyll-*a* product in the *Calimnos* v1.04 data set, which is similar to the result expected in the first climate data record of the Lakes_cci. Further multi-sensor calibration and uncertainty characterization is part of the planned Lakes_cci work.

These results (Figure 10) clearly show that applying the weighted average of a combination of (two) tuned algorithms for each observed pixel provides a marked improvement over selecting, for each lake and each observation day, the algorithm that is most suitable for the lake-wide predominant optical water type. One clearly visible effect is the need to select algorithms that can deal with a (very) high concentration range, likely associated with patchy phytoplankton blooms surrounded by lower biomass conditions. At the scale of the whole lake, bloom-affected pixels are a minority such that mid-range algorithms would perform best for the lake as a whole. A whole-lake algorithm selection can ignore dense (but likely patchy) blooms, shown as saturation at concentrations of

approximately 1000 mg m^{-3}, whereas per-pixel algorithm selection allows retrieval up to two orders of magnitude higher. The dynamic algorithm selection approach is therefore preferred as it is better equipped to deal with optical gradients within individual lakes.

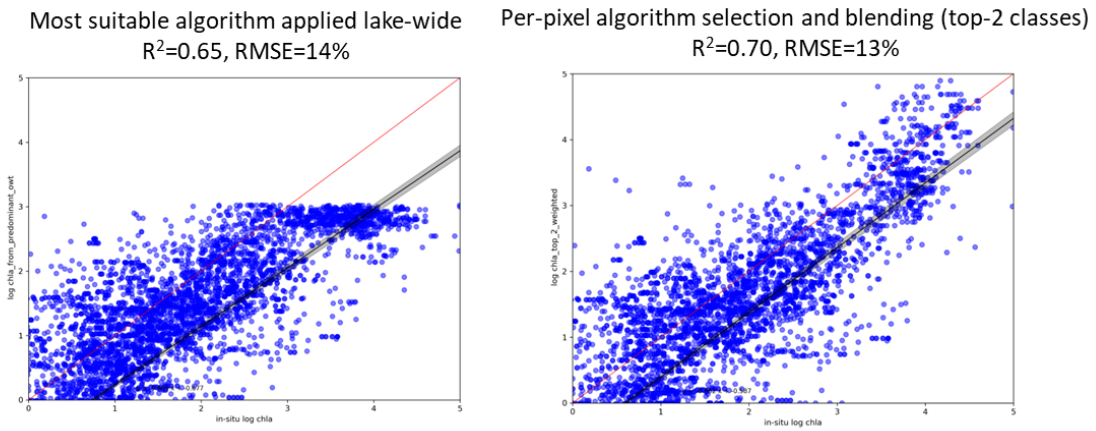

Figure 10: Comparison of the performance of (left) the best chlorophyll-a algorithm for the predominant optical water type of each lake and (right) per-pixel selection and blending of the two highest ranking algorithms based on optical water type membership scores.

5.6 Summary of strengths, weaknesses and limitations

The remarkable variability in the bio-optical properties of inland waters, both regionally and temporally, poses a formidable challenge in developing universally applicable algorithms for atmospheric correction and biogeochemical substance concentration estimates. Numerous studies have highlighted the potential of integrating an OWT classification step in optical complex waters, followed by type-specific algorithm development, regional tuning, or even algorithm switching, to enhance the accuracy of Chla estimates. Our evaluation of a weighted blended Chla product procedure, utilizing the fuzzy OWT classification framework, demonstrates a significant improvement in retrieval performance compared to that of individually regionally tuned algorithms (Figure 10). This outcome aligns with the expected results from the algorithm tuning exercise conducted by Neil et al. (2019) on in situ reflectance data under the same project, as well as the application of individual algorithms to suitable water bodies in their original publications.

The existing water quality algorithms implemented for MERIS and OLCI underwent tuning based on matchups between in situ measurements and MERIS data. This tuning process took into account the extended operational period of MERIS (2002-2012) and the availability of coinciding in situ data from the LIMNADES database. We believe that the similarities in radiometric performance and waveband configuration between MERIS and OLCI enable the extrapolation of the current results to OLCI. However, considering the extended operation time of OLCI and the emergence of new algorithms in recent years, a comprehensive analysis specific to OLCI is necessary.

A thorough evaluation of newly published algorithms in recent years is anticipated for OLCI, and the outcomes will be incorporated in a complete dataset update in the future (V3.0). Additionally, it is worth noting that the current algorithms were tuned using the entire matchup dataset for MERIS. Moving forward, efforts will be made to further tune each algorithm for each assigned OWT by utilizing corresponding representative matchups.

It follows from the above that any change in the upstream processing, either through sensor re-calibration, atmospheric correction improvements or pixel identification, may lead to different estimates in LWLR and derives substances, requiring re-tuning of the algorithm library. This process

is also highly dependent on representative in situ reference observations, which are typically scarce. A regular re-analysis of tuning parameters is therefore recommended.

A known limitation of the methodology described here is an instability in the atmospheric correction step in highly turbid waters, which may lead to unrealistic outcomes. Some of these can be masked and flagged but give rise to a bias in the climate data records towards relatively clearer waters. This is undesirable and being addressed in updates to the algorithm which are being evaluated for future product versions.

5.7 References

Bicheron, P. Amberg, V. Bourg, L. Petit, D. Huc, M. Miras, B. Arino, O. (2011). Geolocation Assessment of MERIS GlobCover Orthorectified Products. IEEE Trans Geosci Remote Sens , 49(8): 2972–2982.

Binding, C. E. J. H. Jerome, R. P. Bukata and W. G. Booty. (2010). Suspended particulate matter in Lake Erie derived from MODIS aquatic colour imagery. International Journal of Remote Sensing 31(19).

Bouvet M. Ramoino F. (2010). Equalization of MERIS L1b products from the 2nd reprocessing, ESA TN TEC-EEP/2009. 521/MB.

Chen, Z., Hu, C. and Muller-Karger, F. (2007). Monitoring turbidity in Tampa Bay using MODIS/Aqua 250-m imagery. Remote Sens. Environ. 109(2): 207-220.

Diversity-II (2015). ESA DUE DIVERSITY II- Algorithm Theoretic Baseline Document (ATBD), Version 2.4, http://www.diversity2.info/products/documents/DEL5/DIV2_Algorithm_Theoretical_Basis_Document_v2.4.pdf.

Gilerson, A. A. Gitelson, A. A. Zhou, J, Gurlin, D. Moses, W. Ioannou, I. and Ahmed, S. A. (2010). Algorithms for remote estimation of chlorophyll-a in coastal and inland waters using red and near infrared bands. Opt Express 18(23): 24109-24125.

Gons HJ, Rijkeboer M, Ruddick KG. (2005): Effect of a waveband shift on chlorophyll retrieval from MERIS imagery of inland and coastal waters. J Plankton Res. 27(1):125-7.

Gordon, H. R. O. B. Brown, R. H. Evans, J. W. Brown, R. C. Smith, K. S. Baker, and D. K. Clark. (1988). A semianalytic radiance model of ocean color. J Geophys Res: Atmos 93: 10909-10924.

Kruse F. A. A. B. Lefkoff, J. W. Boardman, K. B. Heidebrecht, A. T. Shapiro, P. J. Barloon, A. F. H. Goetz. (1993). The spectral image processing system (SIPS)—interactive visualization and analysis of imaging spectrometer data, Remote Sens Environ, 44(2–3):145-163.

Jiang D, Scholze J, Liu X, Simis SGH, Stelzer K, Müller D, et al. (2023). A data-driven approach to flag land-affected signals in satellite derived water quality from small lakes. International Journal of Applied Earth Observation and Geoinformation. 2023;117:103188.

Liu X, Steele C, Simis S, Warren M, Tyler A, Spyrakos E, et al. (2021). Retrieval of Chlorophyll-a concentration and associated product uncertainty in optically diverse lakes and reservoirs. Remote Sens Environ 267:112710.

Miller, R.L. and McKee, B.A. (2004). Using MODIS Terra 250 m imagery to map concentrations of total suspended matter in coastal waters. Remote Sens. Environ. 93(1-2): 259-266.

Mishra, S. D. R. Mishra, Z. Lee, Craig S. Tucker. (2013). Quantifying cyanobacterial phycocyanin concentration in turbid productive waters: A quasi-analytical approach, Remote Sens Environ, 133: 141-151.

Moore, TS. JW. Campbell and Hui Feng. (2001). A fuzzy logic classification scheme for selecting and blending satellite ocean color algorithms. IEEE Transactions on Geoscience and Remote Sens 39(8) 1764-1776.

Morel, A. (1974). Optical properties of pure water and pure sea water. In: Jerlov MG, Nielsen ES, editors. Optical Aspects of Oceanography. New York: Academic Press; 1974. p. 1–24.

Nechad, B. Dogliotti, A. I. Ruddick, K. G. Doxaran, D. (2016). Particulate Backscattering and suspended matter concentration retrieval from remote-sensed turbidity in various coastal and riverine turbid waters. Proceedings of ESA Living Planet Symposium, Prague, 9-13 May 2016, ESA-SP 740.

Nechad, B. Ruddick, K. G, Park, Y. (2010). Calibration and validation of a generic multisensor algorithm for mapping of total suspended matter in turbid waters. Remote Sens Environ 114 (2010) 854–866.

Neil, C. Spyrakos, E. Hunter, PD, Tyler, AN. (2019). A global approach for chlorophyll-a retrieval across optically complex inland waters based on optical water types. Remote Sens Environ 229:159-178.10.1016/j.rse.2019.04.027

Ondrusek, M., Stengel, E., Kinkade, C.S., Vogel, R.L., Keegstra, P., Hunter, C. and Kim, C. (2012). The development of a new optical total suspended matter algorithm for the Chesapeake Bay. Remote Sens. Environ. 119243-254.

Park Y. J. and Ruddick K. Model of remote-sensing reflectance including bidirectional effects for case 1 and case 2 waters. (2005). Appl Optics. 2005; 44(7):1236-49. doi:10.1364/ao.44.001236

Petus, C., Chust, G., Gohin, F., Doxaran, D., Froidefond, J.M. and Sagarminaga, Y. (2010). Estimating turbidity and total suspended matter in the Adour River plume (South Bay of Biscay) using MODIS 250-m imagery. Continental Shelf Research 30(5): 379-392.

Roettgers, R. Doerffer, R. McKee, D. and Schoenfeld, W. (2011). Pure water spectral absorption, scattering, and real part of refractive index model. ESA Water radiance project. From www.brockmann-consult.de/beam-wiki/download/attachments/17563679/WOPP.zip?version=1&modificationDate=1299075673760

Ruescas, A. B. Brockmann, C. Stelzer, K. Tilstone, G. H. Beltran, J. (2014). DUE CoastColour Validation Report (p. 58). Geesthacht, Germany: Brockmann Consult. Retrieved from http://www.coastcolour.org/documents/DEL-27%20Validation%20Report_v1.pdf.

Spyrakos E, O'Donnell R, Hunter PD, Miller C, Scott M, Simis S, et al. (2018). Optical types of inland and coastal waters. Limnol Oceanogr. 63(2). doi: 10. 1002/lno. 10674.

Steinmetz F, Deschamps P-Y, Ramon D. Atmospheric correction in presence of sun glint: application to MERIS. (2011). Optics Express. 19(10):9783-800. doi: 10. 1364/oe. 19. 009783

Steinmetz, F. Ramon, D. Deschamps, P-Y (2016). ATBD v1 – Polymer atmospheric correction algorithm, D2. 3 OC-CCI project http://www.esa-oceancolour-cci.org/?q=webfm_send/658

Steinmetz, F. (2018): ATBD v1 – Evolution of Polymer Atmospheric correction within Copernicus Global Land Service – Inland Water products. On request

Qin P, Simis S, Tilstone GH. (2017). Radiometric validation of atmospheric correction for MERIS in the Baltic Sea based on continuous observations from ships and AERONET-OC. Remote Sens Environ 200:263-80.

Vantrepotte, V. H. Loisel , X. Mériaux, G. Neukermans, D. Dessailly, C. Jamet, E. Gensac, and A. Gardel, (2011). Seasonal and inter-annual (2002-2010) variability of the suspended particulate matter as retrieved from satellite ocean color sensor over the French Guiana coastal waters. J Coast Res. SI 64 (Proceedings of the 11th International Coastal Symposium), – . Szczecin, Poland, ISSN 0749-0208

Warren MA, Simis SGH, Martinez-Vicente V, Poser K, Bresciani M, Alikas K, et al. (2019). Assessment of atmospheric correction algorithms for the Sentinel-2A MultiSpectral Imager over coastal and inland waters. Remote Sens Environ 225:267-89.

Zhang, M., Tang, J., Dong, Q., Song, Q. and Ding, J. (2010). Retrieval of total suspended matter concentration in the Yellow and East China Seas from MODIS imagery. Remote Sens. Environ. 114(2): 392-403.

Zhang, Y. K. Shi, X. Liu, Y. Zhou, B. Qin. (2014). Lake topography and wind waves determining seasonal-spatial dynamics of total suspended matter in turbid lake Taihu, China: assessment using long-term high-resolution MERIS data. PLoS ONE 9(5):e98055. doi:10.1371/journal.pone.0098055.

6 Lake Ice cover – LIC

6.1 Description

Lake ice cover corresponds to the extent (or area) of a lake covered by ice. The generation of a lake ice cover (LIC) product from satellite observations requires implementation of a retrieval algorithm that can correctly label pixels as either ice (snow-free and snow-covered), open water or cloud. From such a product, one can determine ice dates and ice cover duration at the pixel scale (ice-on and ice-off) and lake-wide scale (complete freeze-over (CFO), and water clear of ice (WCI)) (Duguay et al. 2015). From a climate perspective, determination of ice onset (date of first pixel covered by ice), CFO, melt onset (date of first pixel with open water) and WCI are of most relevance to capture important ice events during the freeze-up and break-up periods. Duration of freeze-up and break-up periods and duration of ice cover over a full ice season can be determined from these dates.

The LIC product v2.1 generated for Lakes_cci uses MODIS (Terra and Aqua) data to provide the most consistent and longest historical record globally to date (2000-2022). The full processing chain and retrieval algorithm are described below.

6.2 Algorithm definition

Prior to the main processing chain, the Canadian Lake Ice Model (CLIMo) is applied to help determine which lakes of the Lakes_cci harmonised product (total 2024 lakes) could have formed ice or have remained ice-free at any time over the 2000-2022 period. CLIMo (Duguay et al. 2003) is a one-dimensional thermodynamic model capable of simulating ice phenology events (ice-on and ice-off dates), ice thickness and temperature, and all components of the energy/radiation balance equations during the ice and open water seasons at a daily timestep. Input data to drive CLIMo include mean daily air temperature (°C), wind speed (m s^{-1}), relative humidity (%), snowfall (or depth) (m), and cloud cover (in tenth). Here, ERA5 reanalysis hourly data on single levels (25 km) were used to generate inputs required for CLIMo simulations for each of the 2024 lakes. ERA5 hourly data including wind speed, air temperature, relative humidity, and cloud cover were converted to daily values (each day to be the average of 24 hours). In addition, snow depth of daily accumulation was extracted from the ERA5 hourly data. As a second check to the possible formation of ice on any of the lakes, lake ice depth data provided by ERA5 were also utilised. Ice cover was deemed possible to have formed on a lake if ice depth was determined to have reached a thickness greater than 0.001 m on any day from either CLIMo or ERA5.

Ice was determined to have formed on a common set of 1390 lakes by both CLIMo and from the ERA5 lake ice depth data. 558 lakes were determined not to form any ice (ice-free) from both sources. However, there were also discrepancies between CLIMo simulations and ERA5 ice depth data for 76 of the 2024 lakes. 24 lakes were identified to have formed ice from CLIMo but not ERA5 and vice versa for 52 lakes. Hence, as a third check, a number of lakes (largely located at the southern limit of where ice could potentially form during a cold winter in the Northern Hemisphere and in mountainous regions of both the Northern and Southern hemispheres) were inspected manually through interpretation of MODIS RGB images to determine if any of these lakes had formed ice between 2000 and 2022.

As a result of the process described above, 1391 of 2024 lakes were flagged as forming ice and 633 not forming any ice over the 2000-2022 period. Once flagged, only lakes deemed to form ice were selected to perform lake ice classification from MODIS data by the main processing chain.

An overview of the implemented processing chain is given in Figure 11. It includes three modules: data import, retrieval, and data export. Data is processed one day at a time. As part of global initialization, a water mask is loaded. Then, the data for each day is processed. One execution of the processing chain processes one day of data.

Six MODIS (Terra/Aqua) TOA reflectance bands and a solar zenith angle (SZA) band are used for feature retrieval (i.e. for labelling as water, ice, or cloud) (Wu et al., 2021). The reflectance bands are MOD02QKM/MYD02QKM at 250 m (band 1: 0.645 µm and band 2: 0.858µm) and MOD02HKM/MYD02HKM at 500 m (band 3: 0.469µm; band 4: 0.555µm; band 6: 1.640 µm; band 7: 2.130 µm) resolutions. Geolocation is provided at 1 km resolution and is interpolated to 250 m.

Prior to applying retrieval, pixels of interest are identified as “good” or “bad” using quality bands from the original MODIS TOA reflectance product. The pixels with SZA higher than 85 degrees are identified as “bad”. Pixels of interest are classified and labelled as cloud, ice or water from a random forest (RF) algorithm (Wu et al., 2021). Labelled pixels are resampled to the output grid. The processing chain has been revised for Lakes_cci to generate the output grid based on specifications of the harmonized product. Aggregation is performed by taking a majority vote between ice and water, ties broken by selecting water. If there are zero ice and water pixels, then the cell is labelled as cloud if there are non-zero cloud pixels; otherwise the output cell is labelled as “bad”.

More specifically, the processing steps presented in Figure 11 are:

1. Load TOA reflectance (bands 1, 2, 3, 4, 6, 7 and SZA), geolocation (latitude and longitude), and quality bands as rasters from MODIS Level 1B calibrated radiances product (MOD02/MYD02), Collection 6.1.
2. Identify lake (water) pixels of interest based on maximum water extent from ESA CCI Land Cover (v4. 0) 150-m resolution product.
3. Identify pixel quality and label pixels of interest from application of RF algorithm for the detection of clouds, ice, and open water.
4. Resample labelled pixels acquired in a day from individual swaths to the output grid at 1/120 degrees resolution and perform temporal (daily) and spatial aggregation in terms of each cell in the output grid.
5. Filter the output grid to discard cells (1/120 degrees resolution) which contain land pixels using maximum water extent observed in ESA CCI Land Cover (v4.0) 150-m resolution product.
6. Write and export the daily lake ice cover product in the required format (NetCDF) with metadata.

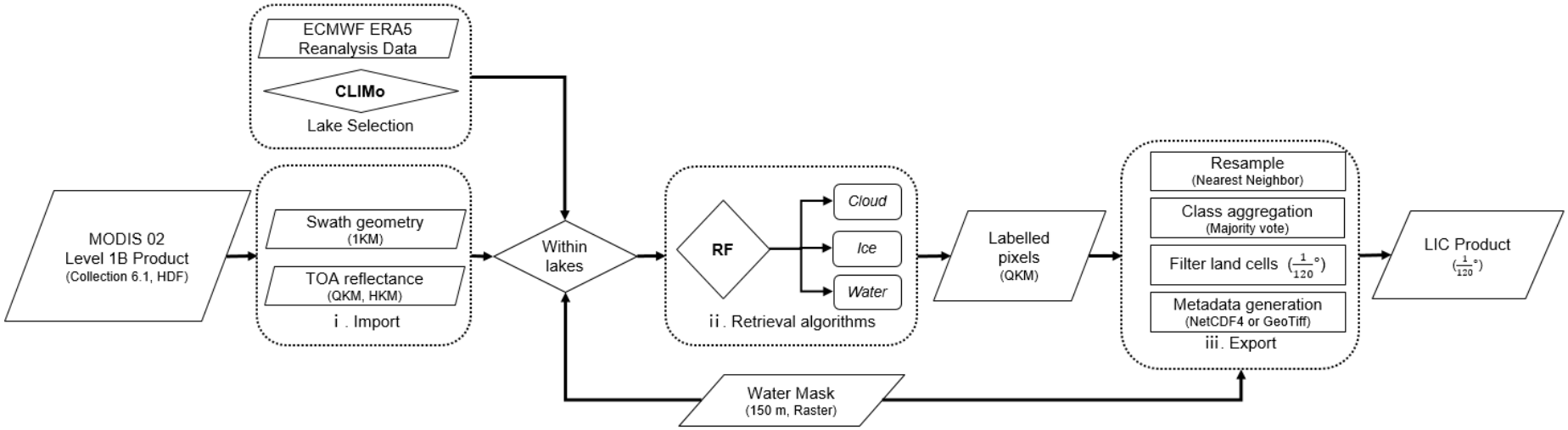

Figure 11: Overview of the processing chain for generation of MODIS LIC daily product. RF stands for random forest

6.2.1 Input Data

Satellite input data:

- MODIS Terra/Aqua Level 1B calibrated radiances product (MOD02/MYD02), Collection 6.1 (TOA reflectance data) stored in two separate files as a function of spatial resolution: MOD02QKM/MYD02QKM (250 m, bands 1-2) and MOD02HKM/MYD02HKM (500 m, bands: 3-4, 6-7). SZA is also used.

Lake water boundaries:

- Maximum water extent observed in ESA CCI Land Cover (v4.0) at 150-m resolution.

6.2.2 Output Data

The output data are produced in the harmonized grid format. The edge of each grid cell subtends 1/120 degrees latitude or longitude. The list of variables included in the LIC product are provided in Table 9.

Table 9: Output variables in LIC product

Band	Variable name	Description	Values
1	lake_ice_cover_class	Label assigned to grid cell	1: water, 2: ice, 3: cloud, 4: bad
2	Lake_ice_cover_flag	Flag assigned to grid cell	1: does_not_form_ice, 2: forms_ice
3	lake_ice_cover_uncertainty	Uncertainty of the label (%); currently determined from accuracy assessment of individual 250-m products (internal evaluation)	0.83: water, 2.23: ice, 3.07: cloud

6.2.3 Retrieval Algorithm

The retrieval algorithm is a RF classifier. As an ensemble approach, RF integrates decision trees developed by bagging samples to improve the limitations of the single-tree structure (Breiman, 2001). The bagging creates several subsets randomly from training samples with replacement (i.e. a sample can be collected several times in the same subset whereas other samples are probably not selected in this subset). Subsequently, each data subset is used to train a decision tree. For building a single tree, a random sample with a number of variables is chosen as split candidates from all variables. The number of variables available to a split is one of key RF hyperparameters, denoted as mtry. For the whole RF model, the number of trees (ntree) is defined a priori to develop various independent classifier outputs. The final class of each unknown sample is assigned by the majority vote of all outputs from the trees.

RF was found to outperform two other machine learning algorithms (multinomial logistic regression, MLR, and support vector machine, SVM) and comparable to gradient boosting trees (GBT) for lake ice cover, open water and cloud classification in a recent paper by the developers of the current LIC product (Wu et al., 2021). While RF and GBT provided similar results following a comprehensive accuracy assessment (cross validation (CV): random k-fold as well as spatial and temporal CV), the former was selected for LIC product generation since it was determined to be less sensitive to the to the choice of hyperparameters necessary for classification compared to GBT, MLR and SVM.

To develop and validate the retrieval algorithm, 17 lakes distributed across the Northern Hemisphere were selected (Figure 12 and Table 10). Training, testing and validation of the four machine learning algorithms found that RF with a combination of visible, near infrared, and mid infrared bands was the best choice for LIC product (Figure 13).

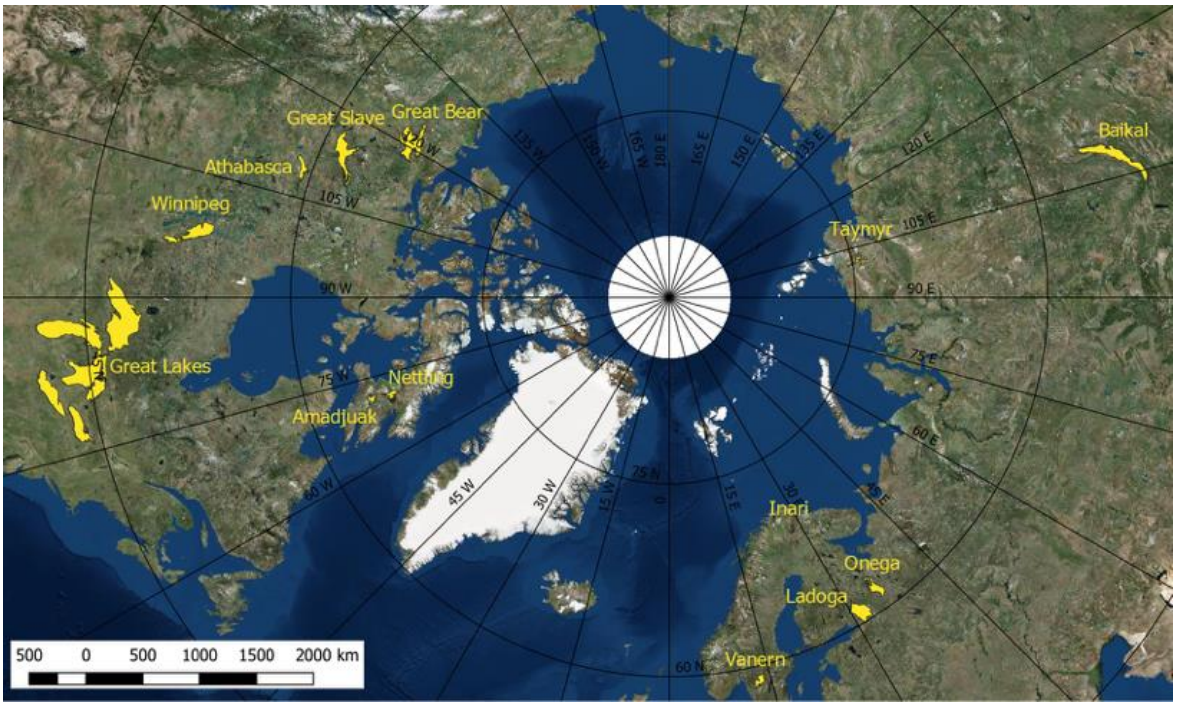

Figure 12: Geographical distribution of lakes used for LIC algorithm development and validation

Table 10: List of lakes for LIC algorithm development and (internal) validation

Lake	Country	Latitude	Longitude	Elevation (m)	Area (km²)
Amadjuak	Canada	64.925	-71.149	113	3,115
Athabasca	Canada	59.424	-109.34	213	7,900
Baikal	Russia	53.525	108.207	456	31,500
Erie	Canada/USA	42.209	-81.246	174	25,821
Great Bear	Canada	66.024	-120.61	186	31,153
Great Slave	Canada	61.579	-114.196	156	28,568
Huron	Canada/USA	44.918	-82.455	176	59,570
Inari	Finland	69.048	27.876	118	1,040
Ladoga	Russia	60.83	31.578	5	18,135
Michigan	USA	43.862	-87.093	177	58,016
Nettilling	Canada	66.42	-70.28	30	5,542
Onega	Russia	61.75	35.407	35	9,890
Ontario	Canada/USA	43.636	-77.727	75	19,009
Superior	Canada/USA	47.945	-87.32	183	82,367
Taymyr	Russia	74.538	101.639	6	4,560
Vanern	Sweden	58.88	13.22	44	5,650
Winnipeg	Canada	52.421	-97.677	217	23,750

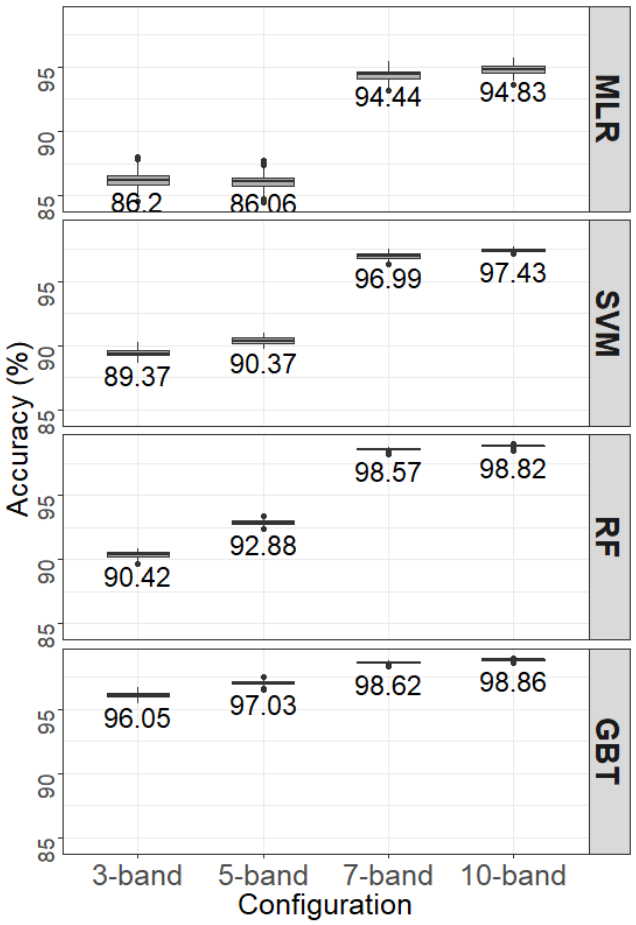

Figure 13: Comparison of classification accuracies (%) obtained with different band configurations across classifiers. The 7-band combination using RF is the one retained for generation of the LIC v2.1 product (Wu et al., 2021)

6.3 Quality assessment

Quality assessment of the LIC product is accomplished by comparing retrieved ice, water and cloud pixels against those obtained from visual interpretation of RGB colour composite images from MODIS Terra Level 1B calibrated radiances (TOA reflectance data). The images are selected to include several lakes across the Northern Hemisphere over a few ice seasons of MODIS Terra record (2000-2022). Other approaches to quality assessment, such as comparison with in situ observations (from lake shore) and satellite-based LIC products generated by other groups is envisaged as part of the CRDP v3.0 release. Uncertainty values reported in LIC are currently derived from overall classification errors for each class (ice, water, and clouds).

6.4 Summary of the strengths, weaknesses and limitations

The random forest algorithm (RF) was selected for LIC product generation since it outperforms threshold-based approaches (e.g., NASA Snow product) and other machine learning classifiers, such as multinomial logistic regression, and support vector machine (Wu et al., 2021). High overall accuracy (>95%) has been achieved with the RF classifier in both spatial and temporal transferability assessments (Wu et al., 2021).

As with any lake product generated from optical data, the presence of clouds as well as extensive cloud cover periods and low solar illumination angles, particularly during the fall freeze-up at high latitudes, introduce classification errors and limit the retrieval of open water and ice cover for many days of the

year. In CRDCP v2.1, highly turbid lakes or sections of lakes have been found to occasionally be misclassified as ice-covered during the open water season. This is also the case for a few lakes that are characterized by snow-free “blue” clear ice during spring break-up; here ice is misclassified as open water.

One limitation of the LIC product is that no retrieval is performed when the solar zenith angle is >85 degrees; a limitation due to the use of MODIS shortwave bands that record very low surface reflectance during ice formation late fall and wintertime. Work is underway to reduce the classification errors described above through the collection of additional training sites at lake locations where misclassification (turbid water as ice cover and melting blue clear ice as open water) has been found to occur. Uncertainty is currently being reported has overall classification error for each class (water, ice, clouds). Improved classification accuracy and provision of per-pixel uncertainty (aleatoric, systematic and total) estimates are planned for CRDP v3.0.

6.5 References

Breiman, L. (2001). Random forests. Machine Learning, 45(1), 5–32. https://doi.org/10.1023/A:1010933404324.

Duguay, C. R. Bernier, M. Gauthier, Y. & Kouraev, A. (2015). Remote sensing of lake and river ice. In Remote Sensing of the Cryosphere, Edited by M. Tedesco. Wiley-Blackwell (Oxford, UK), 273-306.

Duguay, C.R., Flato, G.M., Jeffries, M.O., Ménard, P., Morris, K. & Rouse, W.R. (2003). Ice cover variability on shallow lakes at high latitudes: Model simulations and observations. Hydrological Processes, 17(17), 3465-3483.

Wu, Y., Duguay, C.R. & Xu, L. (2021). Assessment of machine learning classifiers for global lake ice cover mapping from MODIS TOA reflectance data. Remote Sensing of Environment, 253, 112206, https://doi.org/10.1016/j.rse.2020.112206.

7 Lake Ice Thickness- LIT

Lake ice is a major landscape feature in the winter season at northern latitudes and plays a key role in climate moderation and the energy balance (Brown and Duguay, 2010). Lake ice conditions, particularly the length of the ice season and ice thickness, have a significant impact on the economy of northern regions through their influence on transportation, travel, fishing, and recreation activities (Ghiasi et al., 2020). Therefore, accurate knowledge about lake ice properties, such as lake ice thickness (LIT), is necessary. Furthermore, LIT is a key climate change indicator recognized as one of six thematic variables under the GCOS Essential Climate Variable (ECV) Lake. LIT integrates changes in surface air temperature and on-ice snow mass (depth and density) (Brown and Duguay, 2011). Decreasing trends in maximum (late winter) ice thickness have been documented in recent years for lakes on the North Slope of Alaska (ca. 20 cm 1991-2011; Surdu et al., 2014) and in Russia (10-15% decrease 1980-2010; Vuglinsky, 2017). Yet, field LIT measurements are sparse in both space and time, and many northern countries have seen an erosion in their in situ observational networks over the last four decades. Therefore, there is a pressing need to use satellite remote sensing to provide broad-scale and regular monitoring of LIT in the face of climate change (see Murfitt et al 2021 for a recent review).

This section contains a detailed description of a novel physically-based algorithm for the retrieval of LIT founded on the exploitation of Ku-band radar altimetry waveforms in Low Resolution Mode (LRM) that contain information correlated with the seasonal evolution of ice thickness over freshwater lakes. The mathematical formulations, processing steps, input and output data as well as statistical metrics used for quality assessment/validation of each algorithm are provided in the next two sections. A detailed description of the algorithm and results are provided in [Mangilli et al. 2022].

7.1 Description

The radar waveforms from altimetry missions show a specific signature on ice covered lakes. For LRM waveforms, this signature corresponds to a step-like break in the leading edge. This break is understood as the double back-scattering of the radar wave at 1) the snow-ice interface and at 2) the ice-water interface. The width of the step in the leading edge is directly related to the ice thickness. An illustrative example is shown in the right plot of Figure 14 for Jason-3 waveform data over the Great Slave Lake (Canada) in February 2020. When the waveforms, measured along track each ~50 milliseconds (~350 meters), are lined up into a radar echogram, the step-like feature associated with the LIT translates into a distinguishable fringe, as shown in the left plot of Figure 14.

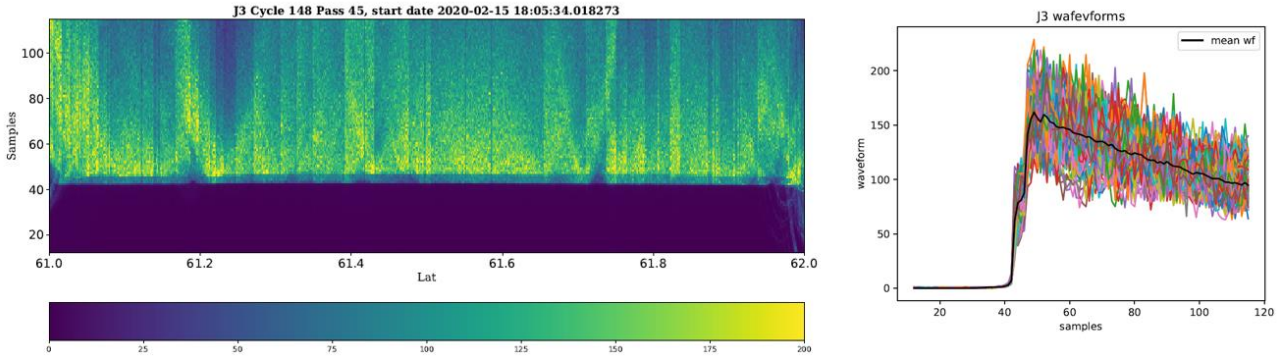

Figure 14: Example of LRM radar echogram (left) and waveforms (right) over the iced-covered Great Slave Lake. Jason-3 data (pass 45, cycle 148, February 2020).

Given the specific signature of the LIT in radar LRM echograms, a physical model can be constructed, based on Brownian modelling of the radar echoes over an ocean surface, where the waveform is described as the sum of two backscattered echoes. The radar waveform, as a function of the range gates, S(x), can therefore be defined as the sum of two positive definite error functions:

$$S_1(\mathbf{x}) = \mathrm{erf}(\mathbf{x} - x_c) + 1$$
$$S_2(\mathbf{x}) = \mathrm{erf}(\mathbf{x} - x_c - \Delta_{ICE}^{gates}) + 1 \qquad [7.1]$$

where x is the range gates array of N gates samples, erf(z) is the error function:

$$\mathrm{erf}(z) = \frac{2}{\sqrt{\pi}} \int_0^z e^{-t^2} dt \qquad [7.2]$$

x_c is the central gate of the first echo and Δ_{ICE}^{gates} is the ice thickness expressed in number of gates, that is, the width of the step in the leading edge. The modelled waveform takes the form:

$$S(\mathbf{x}) = [S_1(\mathbf{x}) + \alpha S_2(\mathbf{x})]\, e^{-\xi \hat{\mathbf{x}}} + N_t, \qquad [7.3]$$

where α= [0, 1] is the amplitude of the second echo, ξ is the parameter associated to the attenuation of the second plateau, modelled as a decreasing exponential, ^x is the normalized samples vector, and N_t is the term associated to the thermal noise. The normalized waveform re-scaled by the overall amplitude A_{wf} , can therefore be modelled as:

$$S_{iced\_lake}(\mathbf{x}, \theta_\mathbf{p}) = A_{wf} \hat{S}(\mathbf{x}) \qquad [7.4]$$

where $\hat{S}(x)$ is the model function of Eq. (7.3) normalized to unit and

$$\theta_\mathbf{p} = \{A_{wf}, \Delta_{ICE}^{gates}, \alpha, \xi, x_c\} \qquad [7.5]$$

is the five parameters vector. The ice thickness in unit of meters, Δ_{ICE}, is defined by applying the following conversion from range gates to meters:

$$\Delta_{ICE} = \Delta_{ICE}^{gates} \frac{c_{ice}}{2B} = \Delta_{ICE}^{gates} \frac{c}{n_{ice} 2B} \qquad [7.6]$$

where B is the radar bandwidth, $c_{ice} = c / n_{ice}$ is the light speed in the ice, with c the speed of light in the vacuum and nice the refractive index of ice.

7.2 Algorithm definition

The LRM LIT algorithm is a retracker specific to the LIT analysis of the radar waveforms, based on the modelling described in section 4.1. For each data cycle, and a given Region of Interest (RoI) defined by a latitude cut $LW_{LIT} = [lat_{min}, lat_{max}]$ over a given target lake, the LIT analysis consists of two steps: 1) the optimization step, that is, the waveform fit, and 2) the estimation of the parameters' mean and standard deviation, as described below and summarized in Figure 15.

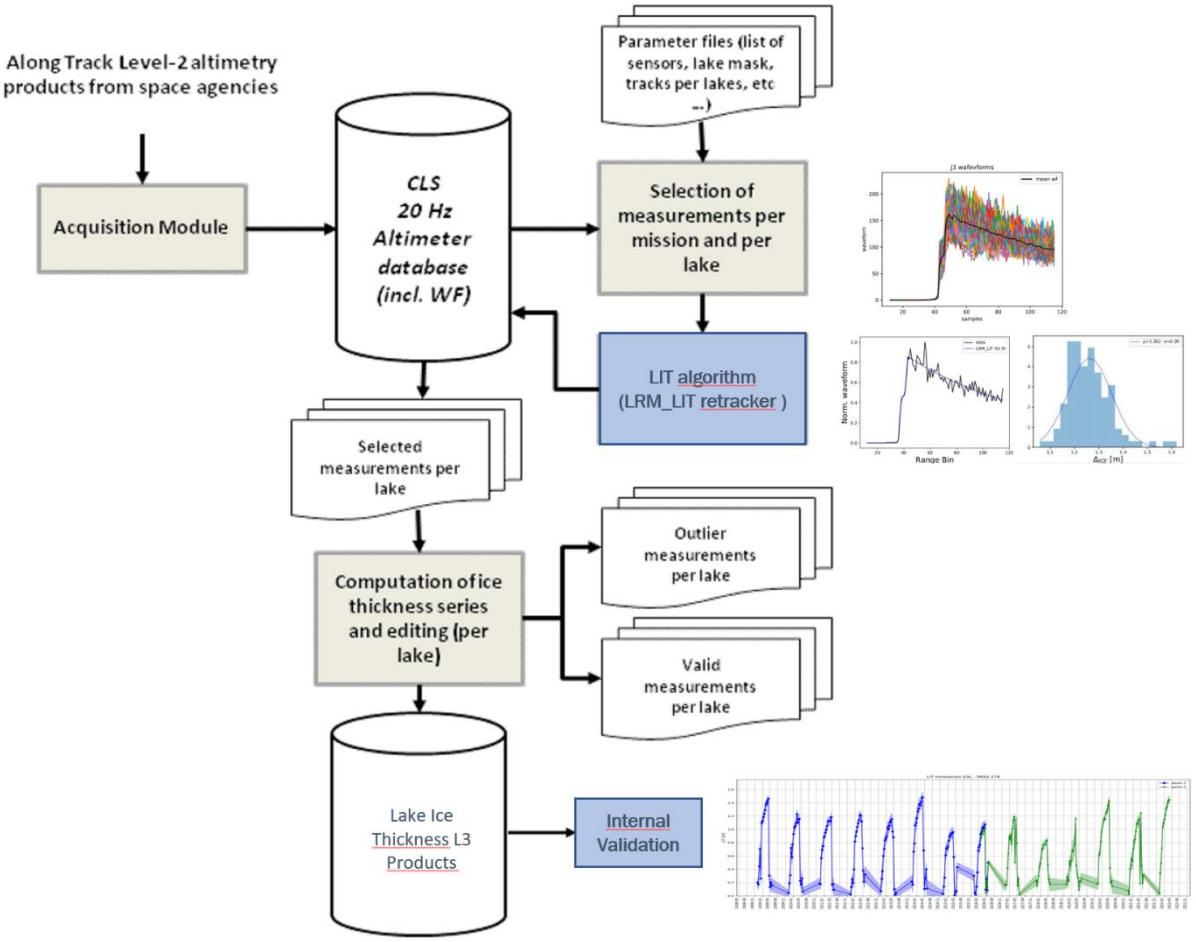

Figure 15: Major steps of the LIT processing

7.2.1 Step 1: Optimisation and best fit parameters

The optimisation step consists of performing a Least Square Levenberg-Marquardt weighted fit of each echo in the LIT analysis window with the model described in 7.1. The optimized function is:

$$\chi^2 = \mathbf{r}^T \mathbb{C}^{-1} \mathbf{r} \simeq \sum_i \left(\frac{r_i}{\sigma_i}\right)^2 \qquad [7.7]$$

where, $r = y(x) - S_{model}(x; \theta_p)$ is the vector of residuals between the waveform data, $y(x)$, and the model, $S_{model}(x; \theta_p)$. The weights, σ_i, are computed as the standard deviation of the echoes within the LIT analysis window. For each data cycle, a set of best fit values for each of the five parameters is provided from the fit of the individual echoes in the analysis window.

7.2.2 Step 2: Parameters estimation and LIT retrieval

The second step of the retracking analysis is the parameter estimation which provides, as the main output, the LIT measurement with the associated uncertainty. The estimation is done by computing the mean and standard deviation of the best fit parameters for each data cycle in the LIT analysis window. To get the constraints on the five parameters with the corresponding uncertainties for each cycle, the histograms of the five parameters best fit values estimated from the fit of each echo is computed. A Gaussian fit on the histograms is performed to get, for each parameter, the mean and variance.

In order to manage eventual outliers, we consider the fit results for which the model and the observations agree within three standard deviations (that is, a reduced chi-squared < 3) . We also discard fit results that could give unrealistic LIT values of Δ_{ICE}>3 meters before computing the LIT histograms and performing the Gaussian fit.

7.3 Quality assessment

7.3.1 Quality checks

We perform reduced chi-squared goodness of fit tests. An example of LIT estimation as a function of latitude along a Jason-2 altimeter track (step 1 of the LRM_LIT retracker) with the reduced chi-squared values for each fitted waveform over Great Slave Lake is shown in Figure 16. Reduced chi-squared values around 1 indicate that the fit performs correctly.

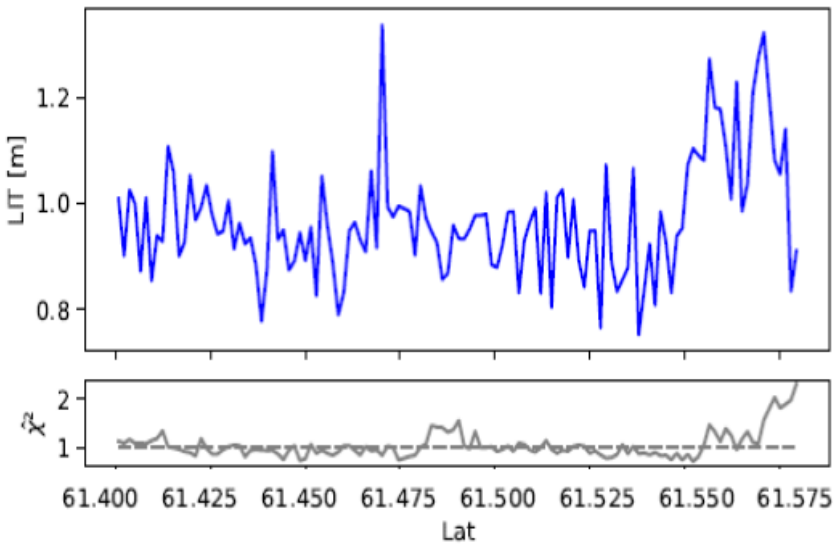

Figure 16: Example of LIT estimation as a function of the latitude along Jason-2 track 45 over the Great Slave Lake (top panel) and the associated reduced chi2 goodness of fit statistics (bottom panel)

7.3.2 Validation

The LRM_LIT retracker has been validated on simulations representative of Jason-like missions. A summary is given in Figure 17, where the top plots refer to winter-like simulated waveforms (left panel) and the LIT histogram (right panel).

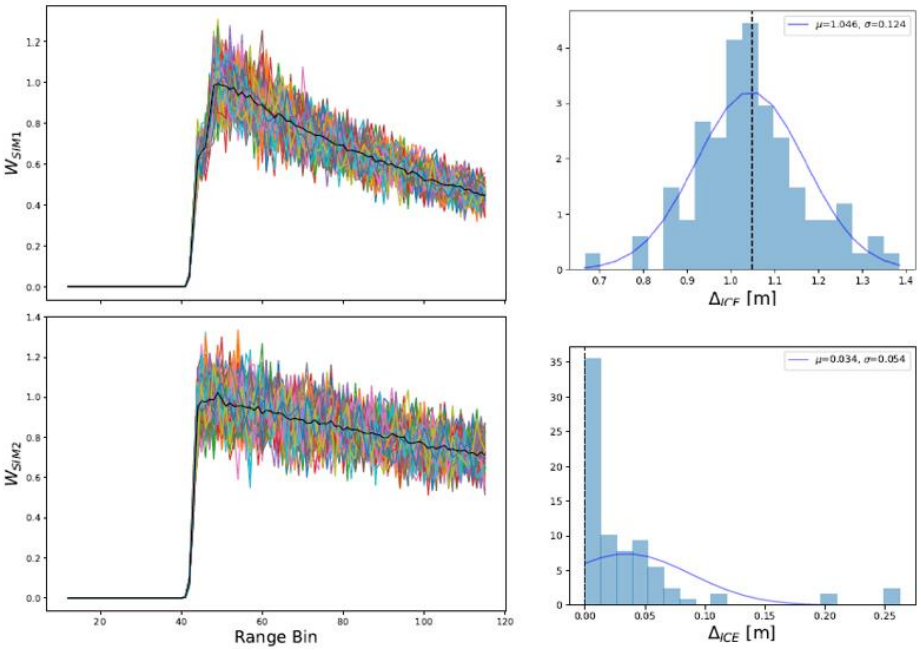

Figure 17: Validation of the LIT estimation with the LRM_LIT retracker on Jason-like simulations. In the left column are shown Jason-like waveform simulations corresponding to the winter-like SIM1 waveforms (top) and to the summer-like SIM2 waveforms. In the right column are shown LIT histograms computed for the winter-like simulations SIM1 (top panel) and for the summer-like simulations SIM2 (bottom panel). The blue lines correspond to the Gaussian fit of the histograms. The input values used to generate the simulations are also shown as dashed black lines.

The input value used to generate the simulations is shown as a dashed line. The same description applies to the bottom plots, for the summer-like simulations without the ice signature. In both cases the LRM_LIT retracker gives unbiased LIT results. The uncertainty of the LIT retrieval from the winter-like simulations is ~10 cm.

LIT retrievals from satellite missions have been evaluated against LIT simulations from the thermodynamic lake ice model CLIMo [Duguay et al., 2003]. A qualitative comparison with in-situ data was also performed when possible[1]. Figure 18 provides an example of the comparison of the LIT estimations obtained within a winter season over Great Slave Lake with the LRM_LIT retracker applied to Jason-2 data (blue triangles) and Jason-3 data (red stars) and LIT from CLIMo simulations with different on-ice snow depth scenarios (diamonds) and in situ data (circles). There is an excellent agreement between Jason-2 and Jason-3 LIT estimates, which are fully compatible with the thermodynamic simulations and qualitatively in agreement with in situ data. We note that, in general, the LIT melting phase is detected earlier with the satellite-based measurements because of snow melting that perturbs the radar echoes.

[1] It is worth noting that the comparison between LIT estimates from satellite missions and in situ data must be taken with caution. In fact, in situ data are collected near the shore, while satellite data are taken from the middle of the lake to avoid land contamination. These are indeed two different environments in terms of bathymetry, wind exposure, snow type and quantity. All these parameters play a key role on ice formation and thickness and they can lead to significant LIT differences.

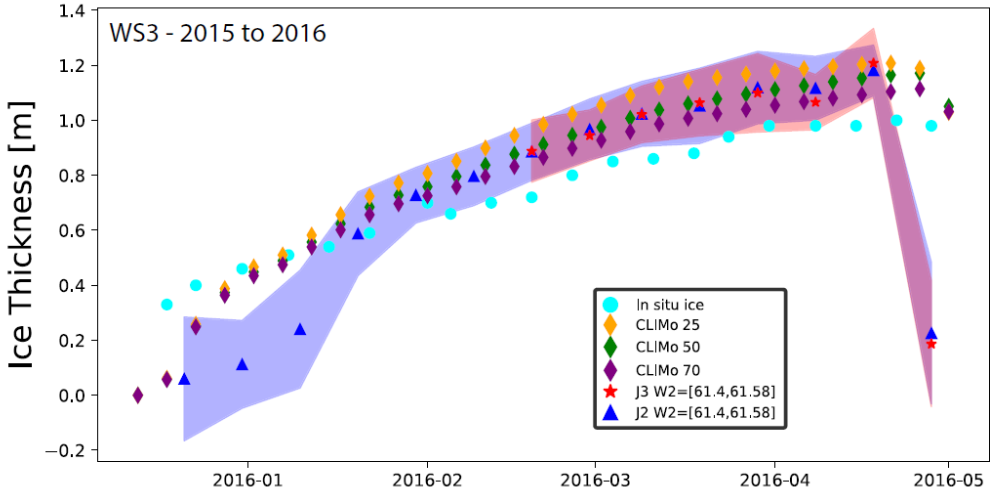

Figure 18: LIT estimates over Great Slave Lake for the 2015-16 winter season. Shown are a comparison between LIT estimates with the LRM_LIT retracker from Jason-2 (triangles) and Jason-3 (stars) data, CLIMo simulations (diamonds) and in situ data (circles). The shaded areas correspond to the LIT estimation uncertainties computed from Jason-2 data (blue) and Jason-3 data (red). Three different realizations of CLIMo simulations are shown by varying the amount of snow on the ice. The in-situ data consist of ice thickness measurements collected in Back Bay near Yellowknife.

To quantify the comparison between the LIT estimates from Jason-2, Jason-3 and CLIMo, two statistics are computed, the MBE:

$$MBE = \frac{1}{N}\sum_{i}^{N}(LIT_i^{J2} - LIT_i^{DS}) \qquad [7.8]$$

And the RMSE:

$$RMSE = \sqrt{\frac{1}{N}\sum_{i}^{N}(LIT_i^{J2} - LIT_i^{DS})^2} \qquad [7.9]$$

of the LIT estimates derived from Jason-2, LIT^{J2}_i , and the other data sets, LIT^{DS}_i , for the N measurements obtained in the middle of the winter season. In the illustrative case of the 2015-16 winter season shown in Figure 18, agreement between the Jason-2 (blue triangles) and Jason-3 (red stars) LIT measurements is excellent. In the middle of the ice season, the MBE is only 0.013 m and the RMSE is 0.024 m between the two data sets. Also, the difference in the LIT mean value is only 0.02 m and that of maximum LIT is 0.025 m. Both Jason-2 and Jason-3 LIT are in strong agreement with the thermodynamics simulations with 50% of snow on ice as input (CLIMo-50 simulations), in particular in the middle of the ice season where the MBE between Jason-2 and CLIMo-50 is less than 0.01 m and the RMSE is 0.019 m. Overall, these results demonstrate that LIT estimates can be retrieved from radar altimetry data that are compatible with thermodynamic simulations and qualitatively in agreement with in situ measurements.

Finally, the superposition of the LIT retrievals on RADARSAT-2 synthetic aperture radar (SAR) and MODIS optical images allows for a better assessment of the consistency of the LIT estimates as they provide valuable information about the state of the ice and overlaying snow cover. Figure 19 shows (left column from top to bottom) the Jason-2 LIT estimates superimposed on RADARSAT-2/MODIS images obtained within one day of Jason-2 overpasses in December, February, March and end of April. The ice thickness is colour coded and ranges from no or thin ice (0-0.32 m) in light blue to LIT in the range of 1.28- 1.60 m in pink. Plots on the right-hand side of Figure 19, show the spatial evolution of the Jason-2 LIT estimates (top plots) and the corresponding evolution of the reduced chi-squared statistics as a function of the latitude (bottom plots) for the same dates as in the left column.

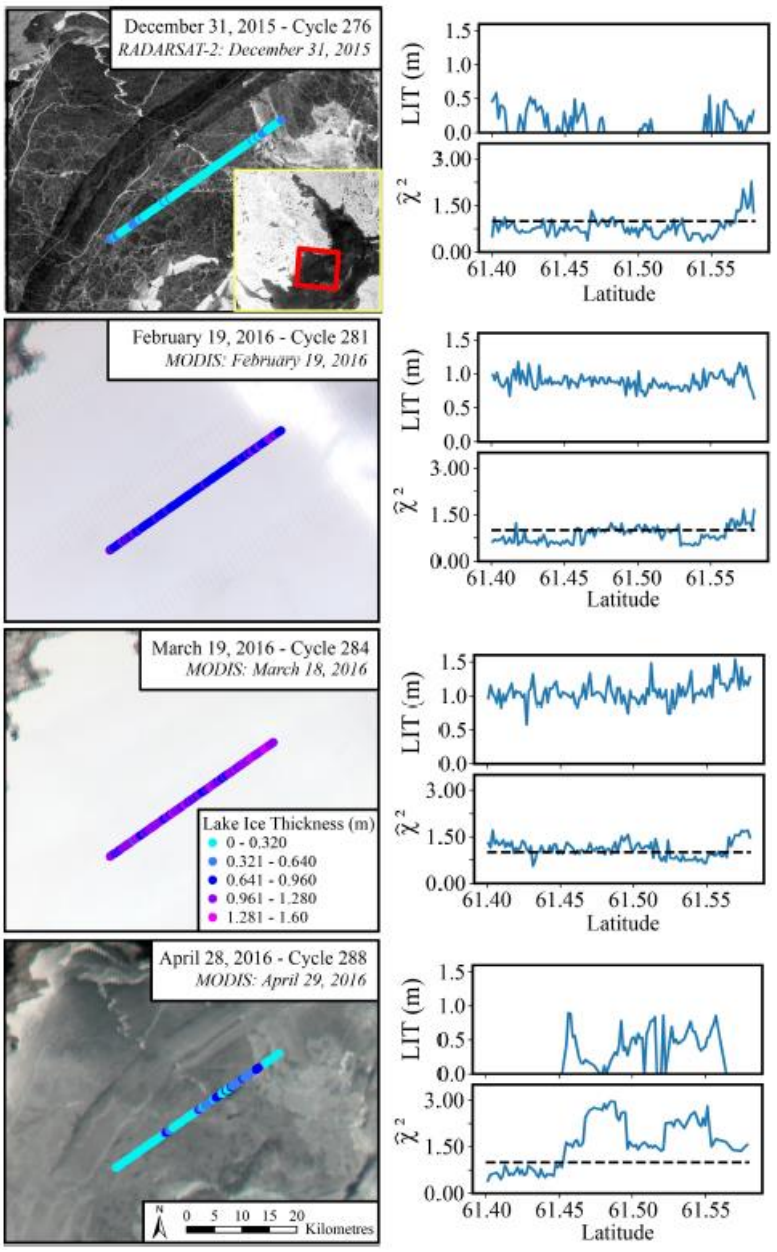

Figure 19 Evolution of Jason-2 LIT estimates over Great Slave Lake along track 45 for WS3 (winter season 2015-2016). Plots in the left column show, from top to bottom, along-track Jason-2 LIT estimates superimposed on MODIS images on the same date or within one day in December, February, March and end of April. Plots in the right column show the evolution of the Jason-2 LIT estimates as a function of latitude (top plots) and of the reduced chi-squared statistics as a function of the latitude(bottom plots) along the track.

7.4 Summary of the strengths, weaknesses and limitations

Overall, the LRM_LIT retracker provides an excellent fit to the data as well as a consistent and robust estimation of LIT over the whole ice growth period. The retracker can capture the inter-annual LIT variations and the seasonal transitions of ice forming and melting but cannot precisely follow the ice evolution at the transitions because of the difficulty of retracking heterogeneous surfaces when the ice is too thin and when snow on the ice surface begins to melt. The accuracy of retrievals, once the ice is well established on the lake surface, is in the order of 0.10 m, providing a significant improvement when compared to previous studies.

The LIT analysis has been illustrated over one representative lake, the Great Slave Lake, but the method can be easily generalized to other target lakes providing that the ice signature, that is, the step like feature in the leading edge, is present in the radar waveforms. Indeed, the freshwater ice signature depends on the properties and thickness of the snowpack and the ice layer and could be erased if some conditions are not met, as for instance in the case of snow-free lake ice or melting snow on the ice surface. In any case, the presence of the ice signature in the radar waveform is a requirement general enough to ensure the robustness of the method over a large number of freshwater lakes. Based on these findings, it can therefore be concluded that the LRM_LIT retracker method is a novel and promising tool for monitoring variability and trends in LIT.

7.5 References

Brown, L.C. & Duguay, C.R. (2010). The response and role of ice cover in lake-climate interactions. Progress in Physical Geography, 34(5), 671–704, doi: 10.1177/0309133310375653

Brown, L.C. & Duguay, C.R. (2011). A comparison of simulated and measured lake ice thickness using a shallow water ice profiler. Hydrological Processes, 25, 2932–2941, doi: 10.1002/hyp.8087.

Duguay, C.R., Flato, G.M., Jeffries, M.O., Ménard, P., Morris, K. & Rouse, W.R. (2003). Ice cover variability on shallow lakes at high latitudes: Model simulations and observations. Hydrological Processes, 17(17), 3465-3483.

Ghiasi, Y., Duguay, C.R., Murfitt, J., Thompson, A., van der Sanden, J., Drouin, H. & Prévost, C. (2020). Application of GNSS interferometric reflectometry for the estimation of lake ice thickness. Remote Sensing, 12, 2721, doi:10.3390/rs12172721.

Kheyrollah Pour, H., Duguay, C.R., Scott, A. & Kang, K.-K. (2017). Improvement of lake ice thickness retrieval from MODIS satellite data using a thermodynamic model. IEEE Transactions on Geoscience and Remote Sensing, 55(10), 5956-5965, doi: 10.1109/TGRS.2017.2718533.

Mangilli, A., Thibaut, P., Duguay, C.R. & Murfitt, J. (2022). A New Approach for the estimation of lake ice thickness from conventional radar altimetry. IEEE Transactions on Geoscience and Remote Sensing, vol. 60, pp. 1-15, 2022, Art no. 4305515 https://doi.org/10.1109/TGRS.2022.3197109

Murfitt, J.C., Brown, L.C. & Howell, S.E.L. (2018). Estimating lake ice thickness in Central Ontario. PLoS ONE, 13(12), e0208519, https://doi.org/10.1371/journal.pone.0208519.

Murfitt, J. & Duguay, C.R. (2021). 50 years of lake ice research from active microwave remote sensing: Progress and prospects. Remote Sensing of Environment, 264, 112616, https://doi.org/10.1016/j.rse.2021.112616.

Surdu, C., Duguay, C.R., Brown, L.C. & Fernández Prieto, D. (2014). Response of ice cover on shallow Arctic lakes of the North Slope of Alaska to contemporary climate conditions (1950-2011): Radar remote sensing and numerical modeling data analysis. The Cryosphere, 8, 167-180, doi:10.5194/tc-8-167-2014.

Vuglinsky, V. (2017). Assessment of changes in ice regime characteristics of Russian lakes and rivers under current climate conditions. Natural Resources, 8, 416-431.